Monthly Notices
of the
ROYAL ASTRONOMICAL SOCIETY

MNRAS **478,** 4238–4254 (2018)
Advance Access publication 2018 May 18

doi:10.1093/mnras/sty1341

Is there a relationship between AGN and star formation in IR-bright AGNs?

Y. Sophia Dai(戴昱),[1,2,3★] Belinda J. Wilkes,[4] Jacqueline Bergeron,[5,6] Joanna Kuraszkiewicz,[4] Alain Omont,[5,6] Adam Atanas,[7] and Harry I. Teplitz[2]

[1]*Chinese Academy of Sciences South America Center for Astronomy (CASSACA), 20A Datun Road, Beijing 100012, China*
[2]*Caltech-Infrared Processing and Analysis Center, 1200 East California Boulevard, Pasadena, CA 91125, USA*
[3]*UCLA, Department of Physics and Astronomy, Los Angeles, CA 90095, USA*
[4]*Harvard-Smithsonian Center for Astrophysics, 60 Garden Street, Cambridge, MA 02138, USA*
[5]*CNRS, UMR7095, Institut d'Astrophysique de Paris, F-75014 Paris, France*
[6]*UPMC Univ Paris 06, UMR7095, Institut d'Astrophysique de Paris, F-75014 Paris, France*
[7]*Picower Institute of Learning and Memory, Cambridge, MA 02139-4307, USA*

Accepted 2018 May 17. Received 2018 May 17; in original form 2017 May 13

ABSTRACT

We report the relationship between the luminosities of active galactic nuclei (AGNs) and the rates of star formation (SF) for a sample of 323 far-infrared (FIR)-detected AGNs. This sample has a redshift range of $0.2 < z < 2.5$, and spans three orders of magnitude in luminosity, $L_X \sim 10^{42-45}$erg s^{-1}. We find that in AGN hosts, the total infrared (IR) luminosity (8–1000 μm) has a significant AGN contribution (average ∼20 per cent), and we suggest using the FIR luminosity (30–1000 μm) as a more reliable star formation rate (SFR) estimator. We conclude that monochromatic luminosities at 60 and 100 μm are also good SFR indicators with negligible AGN contributions, being less sensitive than integrated IR luminosities to the shape of the AGN spectral energy distribution (SED), which is uncertain at $\lambda > 100\mu$m. Significant bivariate $L_X - L_{IR}$ correlations are found, which remain significant in the combined sample when using residual partial correlation analysis to account for the inherent redshift dependence. No redshift or mass dependence is found for the ratio between SFR and black hole accretion rate (BHAR), which has a mean and scatter of log (SFR/BHAR) $= 3.1 \pm 0.5$, agreeing with the local mass ratio between supermassive black hole and host galaxies. The large scatter in this ratio and the strong AGN–SF correlation found in these IR-bright AGNs are consistent with the scenario of an AGN–SF dependence on a common gas supply, regardless of the evolutionary model.

Key words: galaxies: active – galaxies: star formation – infrared: galaxies – X-rays: galaxies.

1 INTRODUCTION

One of the outstanding questions in the study of galaxy formation and evolution is how the presence of a supermassive black hole (SMBH) influences the formation and physical characteristics of the host galaxy. A general connection has been confirmed both locally and at high redshift using empirical correlations between the SMBH mass ($M_\bullet$) and the luminosity, mass, and stellar velocity dispersion of the host (e.g. Kormendy & Richstone 1995; Ferrarese & Merritt 2000; Merloni, Rudnick & Di Matteo 2003). A constant ratio has been found between $M_\bullet$ and the bulge mass (M_{bulge}), measured by several studies to be $\log(M_{bulge}/M_\bullet) \sim 2.9 \pm 0.5$ (Magorrian et al. 1998; Merritt & Ferrarese 2001; McLure & Dunlop 2002; Marconi & Hunt 2003), or $\log(M_{bulge}/M_\bullet) \sim 2.3 \pm 0.3$, after correcting the $M_\bullet$ values by galaxy types (Kormendy & Ho 2013). The scatter of this ratio is found to increase at lower masses ($< 10^{9.5}$ M$_\odot$), and is much larger in bulgeless or pseudo-bulge galaxies than in classical bulge or giant elliptical galaxies, sometimes resulting in no observed correlations for the former types (for review, see Kormendy & Ho 2013). The general galaxy–BH coevolution picture is regardless supported locally by the tight mass correlations, and by the similar cosmic evolution of total star formation rate (SFR) and BH accretion rates (BHARs) up to $z = 3$ (Silverman et al. 2008; Madau & Dickinson 2014).

Despite tremendous progress of the demographic studies of SMBHs, it is still debatable whether, and if so how, the SMBH

★ E-mail: daysophia@gmail.com

regulates the host galaxy formation. Various scenarios exist, sometimes resulting in opposite predictions. The 'feedback' process has been suggested by theories and simulations, in which active BH accretion will suppress and eventually shut down star formation (SF) by heating or expelling the cold gas in the host (e.g. Silk & Rees 1998; Di Matteo, Springel & Hernquist 2005; Bower et al. 2006; Hopkins et al. 2006; Debuhr, Quataert & Ma 2012; Fabian 2012). In the merger-driven model, for example, simulations predict that the merging of two galaxies will boost SF and BH growth, until the feedback from active galactic nucleus (AGN) quenches the SF, especially from luminous AGNs (e.g. Di Matteo et al. 2005; Hopkins et al. 2006; Treister et al. 2012). Besides the merger model, in several competing theories the BH and galaxy grow in tandem via accretion and SF, especially for less-luminous AGNs (e.g. Springel et al. 2005; Dekel et al. 2009; Klypin, Trujillo-Gomez & Primack 2011; Fanidakis et al. 2012). Secular processes, internal to the galaxy, may lead to concurrent galaxy and BH growths based on a common gas supply, at lower galaxy mass (e.g. Springel et al. 2005). Steady cold gas flow along cosmic filaments or quasi-hydrostatic dark matter haloes can contribute to the in situ BH accretion and star formation, but energy feedback from AGNs or supernovae is often needed to regulate this process (e.g. Lilly et al. 2013; Lapi et al. 2014; Aversa et al. 2015; Mancuso et al. 2016). Despite all the simulation progress, which shows that cosmic cold gas flows likely contribute to galaxy growth and eventually the BH growth, the mechanism whereby this material reaches or is ejected from the centre is not yet fully understood (e.g. Bournaud et al. 2011; Gabor & Bournaud 2013; Naab & Ostriker 2017). In all scenarios, the connection between the central AGN and the star formation is a key parameter to characterize the different models.

Recent studies have tried to directly trace the global properties of AGNs and their host galaxies via correlations between their intrinsic luminosities and their star formation rates (e.g. BHAR and SFR). Given the differences in spatial scales between AGN ($\sim$100 pc) and SF (up to tens of kpc), any observed correlation would indicate an intrinsic connection (Alexander & Hickox 2012; Kormendy & Ho 2013). The AGN luminosities are often traced by X-ray luminosities (L_X) or optical emission lines. Optical indicators (e.g. [O III] and [O I]) are generally limited to narrow line regions with good spectral coverage, and thus dominated by local type 2 AGNs (AGNs with signs of obscuration) or Seyferts (e.g. Netzer 2009; Diamond-Stanic & Rieke 2012; Matsuoka & Woo 2015). The X-ray-based AGN luminosities are generally more reliable than the bolometric luminosity based on optical continuum, as the latter may still suffer from obscuration. As a result, the X-ray luminosity, which is dominated by nuclear emission, is more widely used as an AGN indicator, where AGNs are commonly defined as systems with $L_X > 10^{42}$ erg s^{-1} (e.g. Szokoly et al. 2004; Hasinger 2008). As will be discussed below, two outstanding factors affect the observed AGN–SF relations: the method used to derive the SFR; and the sample selection effects.

1.1 SFR indicators

Commonly used SFR indicators range from emission lines (e.g. Hα), ultraviolet (UV) luminosities, to luminosities in the mid-infrared (mid-IR) and total IR bands (e.g. Kennicutt 1998). Unfortunately, all these methods have their weaknesses. SFR inferred from optical emission lines are generally more reliable, as they probe SFR on shorter timescales than the integrated UV or IR luminosities. This method, however, suffers from limited sample size, as emission line observations are time consuming, especially for high-z sources (e.g. MOSDEF, McLean et al. 2012). SFRs inferred from both UV and mid-IR luminosities can be dominated or heavily contaminated by the AGN emission. Without AGN removal, this results in overestimated SFRs as well as the total-IR luminosity in these bands. In this study, for SFR indicator, we choose to use the far-IR (FIR) luminosity. The far-IR emission traces the cold dust and provides a less contaminated measure of SFR in an AGN. Besides integrated $L_{\rm FIR}$, another common practice is to use a single FIR band luminosity as the SFR proxy (e.g. *Herschel* PACS or SPIRE), typically νL_ν (60 μm) (e.g. Netzer 2009; Shao et al. 2010; Rosario et al. 2012, 2013b; Santini et al. 2012), or at longer wavelengths (e.g. 90 μm, 100 μm; Matsuoka & Woo 2015). This is based on the assumption that at rest-frames greater than 50 μm, the AGN contribution is insignificant. However, the amount of the intrinsic AGN emission in the rest-frame FIR remains uncertain at $\lambda > 40$–50 μm (Dai et al. 2012; Podigachoski et al. 2015). For instance, by comparing different AGN spectral energy distribution (SED) templates, from Elvis et al. (1994), Richards et al. (2006), Netzer et al. (2007), Mullaney et al. (2011), Dai et al. (2012), Dale et al. (2014), we found an intrinsic variation of up to 0.9 dex at 60 μm between different AGN models (normalized at 6 μm). Observationally, recent studies on local AGNs ($z < 0.05$) reported a FIR flux excess, possibly associated with AGN activity (e.g. Shimizu et al. 2016). This motivates the use of the full SED to deconvolve the AGN and SF contributions in several recent studies (e.g. Chen et al. 2015; Stanley et al. 2015; Shimizu et al. 2017; Azadi et al. 2017) as well as in this work (Section 3.1). Even studies using (far-) IR-based SFR report different, sometimes contradictory correlations (or lack of). The situation remains far from clear.

1.2 Sample selection methods and notes on scatter

AGN samples are typically selected in three bands: X-ray, optical, and IR (Padovani et al. 2017). The majority of the AGN–SF correlation studies utilize X-ray-selected AGN samples, which are then matched to IR or sub-mm data. Earlier studies based on X-ray and single band sub-mm detections found a luminosity-dependent AGN–SF relation up to $z \sim 2.5$: significant correlation between L_X and SFR from $\nu\, L_\nu(60)$[1] in the most luminous ($L_X > 10^{44}$ erg s^{-1}) AGNs; but no correlation at lower luminosities (or $z > 1$) (Lutz et al. 2010; Shao et al. 2010; Rosario et al. 2012; Santini et al. 2012). Common interpretations of these results invoke different mechanisms at high and low AGN luminosities: major mergers dominate the luminous end, triggering simultaneous BH accretion and starburst episodes; while secular evolution is responsible for the growth of the majority of galaxies with moderate nuclear activity. In the latter, non-merger-driven SF occurs in step with SMBH accretion, possibly fuelled by the same gas reservoir, regardless of AGN activity, BH/host mass, or the level of obscuration (e.g. Lutz et al. 2010; Rosario et al. 2012; Mullaney et al. 2012b). Evidence of coeval AGN–SF evolution has also been found in massive galaxies, regardless of the level of SMBH accretion (Podigachoski et al. 2015), and in AGN samples of X-ray and FIR detections with SED-based SFR (Xu et al. 2015a). Similar luminosity-dependent relations have also been observed between the AGN subtracted specific SFR (sSFR = SFR divided by stellar mass, M_*) and L_X, where no correlation was found at $L_X < 10^{43-43.5}$ erg s^{-1} and $z < 1$ (Rovilos et al. 2012; Santini et al. 2012). Stacking of the IR-undetected

[1]Except Lutz et al. (2010), where SED based on 870 μm observation was used to derive the SFR.

AGNs is a common practice. It is worth noting that the majority of the stacked results are similar, with either a luminosity-dependent correlation that flattens towards the less luminous end (Lutz et al. 2010; Shao et al. 2010; Rosario et al. 2012) and lower specific L_X (L_X/M_* Bernhard et al. 2016), or no overall correlations (Harrison et al. 2012; Mullaney et al. 2012b; Stanley et al. 2015). Similar flatter correlation, or no SFR enhancement compared to regular main-sequence (MS) galaxies, are observed in AGNs detected in both X-ray and FIR, both locally ($z < 0.05$, Shimizu et al. 2017) and at $0.5 < z < 2.5$ (Mullaney et al. 2012b).

In contrast, some studies have found that X-ray-selected AGNs show a strong negative relation between L_X and far-IR flux/luminosity. This can be interpreted as suppressed host SF from AGN feedback (Page et al. 2012; Barger et al. 2015; Shimizu et al. 2015). Analysis of a larger sample showed that the Page et al. (2012) result was biased by the limited sample size and cosmic variance (Harrison et al. 2012). Nevertheless, more recently, suppressed SF, possibly due to AGN feedback, has been reported, either in the form of declining flux at 850 μm towards higher L_X in quasars at $z > 1$ (Barger et al. 2015), or with AGNs, mostly Seyferts and low-ionization narrow-line emission radio galaxies (LINERs), lying below the MS galaxies at $z < 0.05$ (Shimizu et al. 2015).

Intrinsic X-ray obscuration makes the situation more complicated. The obscuration is due to one or several of the following factors: (1) orientation-dependent obscuration related to the central disc/torus-like geometry (e.g. unification model, Barthel 1989; Antonucci & Miller 1985); (2) other nuclear material, such as the narrow emission-line region, lying in a ∼polar orientation; (3) material along the line of sight through the host galaxy (Goulding et al. 2012). Obscuration decreases the X-ray emission at soft energies, reducing the observed flux, and thus X-ray-selected AGN samples retain a bias against obscured sources. Observationally, several studies have noticed a lack of correlation between (s)SFR and the obscuration (represented by the Hydrogen column density, N_H) levels (Lutz et al. 2010; Shao et al. 2010; Rosario et al. 2012; Rovilos et al. 2012). Low levels of obscuration ($N_H \lesssim 10^{23}$ cm^{-2}) can be estimated from the observed hardness ratio (HR) for sources with known redshift. However, as the obscuration of the primary X-ray power-law component increases, weaker soft X-ray components dominate the emission so that the HR no longer traces the level of obscuration (Wilkes et al. 2013). Low-frequency radio (e.g. 3CR) and high-energy X-ray samples, which have little/no orientation bias, find that ∼50 per cent of active galaxies are obscured with ∼50 per cent of these being Compton thick [$N_H \sim 10^{24-26}$ cm^{-2}, Wilkes et al. (2013); Lansbury et al. (2015); Brightman et al. (2016); Lansbury et al. (2017)]. The 'observed' X-ray luminosities of high-redshift (z∼1−2), high-luminosity 3CR sources are ∼100−1000 × lower than their unobscured counterparts for the most highly obscured (∼Compton Thick, $N_H \lesssim 10^{24}$ cm^{-2}) sources (Wilkes et al. 2013), and a subset will fall below the flux limit and be lost from the sample altogether. For those that remain in the sample, hardness ratios underestimate the obscuration levels, and thus the intrinsic X-ray luminosities for ∼25−50 per cent are also underestimated by 1–3 dex. This effect increases towards lower redshift as the observed band moves towards lower energy. Without accounting for these uncertainties, it is difficult to draw conclusions on the presence/not of a relation between X-ray-based AGN luminosities and SF.

For optically selected AGNs, on the other hand, different correlations have also been observed. Positive correlations between L_{AGN}, traced by [O III] and [O I] lines, and single band far-IR luminosities (60, 90, 100 μm), have been observed in local ($z < 0.2$), type 2 AGNs (Netzer 2009; Matsuoka & Woo 2015). For broad-line, optical type 1 quasars, Rosario et al. (2013b) noticed an overall lack of 60 μm-based SFR enhancement in AGN hosts at $0.3 < z < 2.1$, but recent studies found that this might vary with the level of star-formation. Up to $z \sim 3$, SFR increases with increasing optical-based L_{AGN}, [C IV] line-width, and SMBH mass for moderate star-forming AGNs (SFR $\sim 300\,M_\odot$ yr^{-1}, Harris et al. 2016), but remains constant in starburst AGNs (SFR $> 1000\,M_\odot$ yr^{-1}) with higher L_{AGN}, Eddington ratio, and SMBH mass (Pitchford et al. 2016).

Finally, selecting AGNs from star-forming galaxies, i.e. by IR flux or luminosity, has resulted in mainly positive correlations between BHAR and SFR regardless of AGN luminosity ($L_{AGN} = 10^{43-47}$ erg s^{-1}). This correlation exists in both X-ray-selected star-forming AGNs with or without stacking the non-detections (Symeonidis et al. 2011; Chen et al. 2013), and in optical- or IR-selected star-forming AGNs (Chen et al. 2015, Xu et al. 2015a,b). A positive correlation suggests two possible scenarios of AGN/SF coevolution: either a strong cold gas inflow is fuelling the BH accretion and galaxy SF simultaneously, or a merger-triggered nuclear starburst with strong accretion during the early encounter (Hopkins 2012). Recent work combining X-ray, optical and IR AGN selections did not find an AGN–SF (or BHAR–SFR) correlation, but an observed SFR bias by the AGN selections, with IR AGNs being more star-forming than optical AGNs, and no SFR preference in X-ray-selected AGNs (Azadi et al. 2017).

Regardless of how AGN samples were selected, studies of various galaxy populations have found AGNs lying mostly along the star-forming galaxy MS, within a relatively narrow range in the ratio of SFR to M_* (e.g. Noeske et al. 2007; Elbaz et al. 2007, 2011; Pannella et al. 2009; Rodighiero et al. 2011; Speagle et al. 2014; Stanley et al. 2017). Despite the general increase in SFR of the star-forming galaxy MS towards higher redshifts, AGNs reside mainly in MS hosts exhibiting SFR and stellar mass similar to those of inactive star-forming galaxies in $0 < z < 3$. A small fraction (<10 per cent) of AGNs show enhanced average host SFR (e.g. Mullaney et al. 2012a; Rovilos et al. 2012; Santini et al. 2012; Rosario et al. 2013a,b). A positive correlation has also been found between L_{AGN} and circumnuclear SFR in local Seyfert galaxies (Diamond-Stanic & Rieke 2012; Esquej et al. 2014; García-González et al. 2016). Recent studies on long-term BHAR indicates that the apparent parallel growth observed for BHs and host galaxies may be primarily due to a joint dependence on stellar mass, in that the average SFR and BHAR are both larger in higher mass galaxies (Yang et al. 2017).

Simulations show that a 'real' AGN–SF correlation may be masked by the large scatter, possibly affected by various factors: the AGN evolutionary stage of the sample included (e.g. for major mergers, the relation may differ before/during/after merging), the variability time-scales of AGNs and SFR; and the Eddington ratio (ER) distributions in the samples (e.g. Hickox et al. 2014; Stanley et al. 2015; Volonteri et al. 2015b). For example, a flat or non-correlation becomes significant and positive when average instead of instantaneous L_X is used (Azadi et al. 2015); while the inclusion of upper limits or stacking may flatten the observed trend (e.g. Stanley et al. 2015). It is important to bear in mind that not all IR-bright galaxies are AGNs, e.g. only 10–30 per cent of the (ultra-) luminous IR galaxies – (U)LIRGs – are AGNs (e.g. Fu et al. 2010; Hopkins 2012), and vice versa, not all AGNs are IR-bright. Moreover, the different ways of projecting the correlations may also affect the outcome. Data points are often binned to overcome poor statistics in assessing the trends, but this binning can introduce its own biases in the results. For example, L_X and SFR are not as strongly correlated

when binned by AGN luminosity or BHAR as when binned by SFR – a result that can be explained by the shorter time-scales of AGN variability (e.g. Gabor & Bournaud 2013; Hickox et al. 2014; Chen et al. 2015; Volonteri et al. 2015a). Besides, as mentioned earlier, the way of measuring SFRs could also introduce systematics.

1.3 This paper

The aim of this paper is to test the different galaxy evolution scenarios via the AGN–SF connection with a statistically significant sample of active galaxies, undergoing both active AGN and star-forming activities. Since (i) X-ray surveys are typically dominated by AGN down to $L_x \lesssim 6 \times 10^{-18}$ erg cm^{-2} s^{-1} (Luo et al. 2017), and are less biased against edge-on/obscured sources than optical surveys, and (ii) using full SED including FIR data yields a more reliable SFR estimate for AGN systems, in this work we choose to focus on IR-bright, X-ray-selected AGNs that are detected in both the X-ray and FIR. This sample is selected from the 11 deg^2 X-ray multimirror mission (*XMM*)–*Newton* large scale structure (*XMM*–LSS) field, and all of them have known redshifts. In Section 2, we describe the multiwavelength data and the AGN selection; in Section 3 we calculate the L_{IR}, SFR, SMBH mass, and Eddington ratios; we then discuss our results and their implications in Section 4, followed by a summary in Section 5. In this work, we assume a concordance cosmology with $H_0 = 70\,\mathrm{km\,s^{-1}\,Mpc^{-1}}$, $\Omega_M = 0.3$, and $\Omega_\Lambda = 0.7$.

2 THE SAMPLE

To focus on the AGN phase where both BH accretion and SF are active, we selected a sample of AGNs detected in both hard X-ray (2–10 keV) and FIR (250 μm) with redshifts and multiwavelength photometry for SED and luminosity estimates.

We started with the 10 ks *XMM*–LSS X-ray deep full exposure catalogue (XLSSd, Pierre et al. 2007; Chiappetti et al. 2013, C13). The nominal flux limits (50 per cent detection probability) are 3×10^{-15} erg s^{-1} for the soft band (0.5–2 keV), and 1×10^{-14} erg s^{-1} for the hard band (2–10 keV) over the survey region. We restricted our sample to the 2399 hard X-ray-detected objects with either spectroscopic and/or photometric redshift (*Parent sample*), which consist of 75 per cent of the 3194 hard X-ray-detected objects in the field. The remaining 795 objects have no z information due to the non-uniform multi-wavelength coverage of the field. These objects with no redshift estimate share a similar X-ray flux distribution but are generally fainter in the optical and IR. We did not limit our sample to optical point-sources, as extended optical morphologies have also been reported to be common in IR-detected AGNs (Dai et al. 2014). For 50 per cent (1190) of the selected hard X-ray targets, spectroscopic redshifts (spec-z) are available from:

(a) the SDSS-BOSS DR12[2] catalogue (943, within a matching radius of 6″),

(b) various publications (229,[3] for detailed reference list see Melnyk et al. (2013), M13),

(c) an MMT-Hectospec redshift survey based on 24 μm priors (18, see survey selection described in Dai et al. (2014)).

In parentheses are the numbers of unique spectra in these catalogues. The remaining 50 per cent (1209) objects have photometric redshifts (photo-z) reported in M13.

We then matched the parent sample to the HerMES DR3 and DR2 catalogues[4] (Roseboom et al. 2010, 2012; Oliver et al. 2012; Wang et al. 2014) and identified 382 AGNs with 250 μm detections ($>3\sigma$). The HerMES *XMM*–LSS SWIRE field covers 18.87 deg^2 and has a 1σ sensitivity of 5.6 mJy (instrumental + confusion noise) at 250 μm (Wang et al. 2014). A matching radius of 10 arcsec, between the 6arcsec PSF for *XMM* and the 18 arcsec PSF for Herschel-SPIRE1 (250 μm), was chosen to maximize the matching counts while minimizing random associations to be <1.5 per cent.

The rest frame, hard-band X-ray luminosity (derived from 2–10 keV, hereafter referred to as L_x) was determined assuming a photon index, $\alpha_\nu = 1.7$ and $N_H(\mathrm{Gal}) = 2.6 \times 10^{20}$ cm^{-2} (Chiappetti et al. 2013; C13). X-ray hardness ratios: $HR = (H - S)/(H + S)$, where S is defined as the net counts in the soft band, 0.5–2 keV, and H is the net counts in the hard band, 2–10 keV, were determined from the net counts from C13. L_X was corrected for obscuration based on the observed HR for each source detected in both bands, and for which $HR < -0.5$. In this step we assumed an intrinsic power-law spectrum with the same α_ν and N_H(Gal) values above. For the 50 obscured sources with no soft band detection, X-ray lower limits on the absorption corrected luminosity were determined by adopting a conservative upper limit to the soft band count rate of 0.005 ct s^{-1} [table 6 in Pierre et al. (2007)]. As discussed in Section 1, the corrected X-ray luminosities remain a likely lower limit as we cannot rule out the presence of an additional, soft component in these low signal-to-noise data. In addition, neither the total counts nor individual background estimates is available in C13, so we were unable to determine the statistical errors on the individual HR. As shown in Aird et al. (2015, see their fig. 5), the errors on the X-ray luminosity estimate for sources with obscuration levels $\geq 10^{23.5}$erg s^{-1} can be ∼1 dex. To estimate the maximum level of error on our luminosity calculations, we assumed that the top 10 per cent most luminous sources were unobscured at given redshift bins, and used their average value as an upper limit for the intrinsic luminosity. This was done with a z bin size of 0.4. We then calculated the L_X uncertainties for the lower luminosity (obscured) sources individually, following the above assumption. The median and deviation of the L_X uncertainty calculated this way are $\sim 0.6 \pm 0.4$ dex. These values provide a conservative estimate for the L_X errors. For a more realistic estimate, we adopted an effective L_X upper limit based on the observed 6 μm luminosity, following equation (1) introduced in Section 3.1, which has an intrinsic $1\,\sigma$ scatter of 0.3 dex. The majority of the L_X uncertainty estimated this way has a median of 0.3 dex, with a $1\,\sigma$ deviation of 0.4 dex, and a maximum value of 1.7 dex. After adding the intrinsic scatter from the IR-L_X conversion, these values are comparable with the (0.6 ± 0.4) dex calculated above.

Of the 382 AGNs with a *HerMES* detection, 328 are obscuration-corrected, including 28 optical type 1 AGNs that are X-ray obscured. Most optical type 1 sources are unobscured ($HR < -0.2$, $N_H < 10^{22}$ cm^{-2} for $z \sim 2.5$ and $\Gamma \sim 2$, Hasinger (2008)). A total of 166 (43 per cent) objects have $HR > -0.2$ and are defined as X-ray obscured (correction factor >1). For the remaining 216 sources that are not X-ray obscured, the L_X errors are ∼15−25 per cent due to statistical errors combined with the uncertainty in the spectral

[2] http://skyserver.sdss.org/dr12

[3] Not counting the 301 objects with SDSS BOSS spectra in part a, of which the redshifts are consistent in >97 per cent of the cases, and the spec-z from SDSS was used.

[4] http://hedam.lam.fr/HerMES/

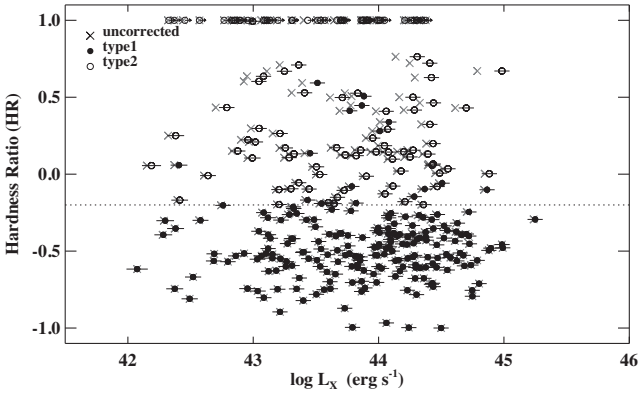

Figure 1. The obscuration corrected (circles) and uncorrected (crosses) L_X versus Hardness Ratio (HR, for definition, see Section 2) of the main sample. Filled circles mark the unobscured 'type 1' AGNs (X-ray unobscured, HR < -0.2, or optical type 1), and open circles are the obscured 'type 2' AGNs (X-ray obscured, HR > -0.2). About 14 per cent of the main sample has an X-ray lower limit. The dotted line marks the X-ray separation between type 1 and type 2 AGNs at HR $= -0.2$ (Szokoly et al. 2004). Above this dotted line, ∼15 per cent of the X-ray obscured sources show broad optical line features and qualify as type 1 objects.

slope. Fig. 1 shows the HR and L_X distribution of the main sample (defined below).

In this study, we focus on the 323 far-IR-detected X-ray AGNs with $L_X \geq 10^{42}$erg s^{-1} and at $0.2 < z < 2.5$ (**main sample**, Table 1). Because of the requirement of FIR detection, hereafter we will refer to this main sample as IR-bright AGNs. This sample is reached after removing 26 sources with $L_X < 10^{42}$erg s^{-1} and 33 IR-bright AGNs outside this redshift range. The redshift limits are motivated by the concerns that (1) at low z ($z < 0.2$) targets are more susceptible to obscuration because the observed energy range is lower. In fact, the absorption correction factor is on average ∼15 per cent higher below this z cut. In addition, our subsample at $z < 0.2$ has a $>2\times$ larger dynamical luminosity range than at higher redshift, with many sources below the 10^{42} erg s^{-1} cut; (2) high z targets are limited by small number statistics. The median and mean redshifts of the main sample are $z = 0.94$ and 1.04, respectively. About 60 per cent of the main sample have spec-z (142 from BOSS, 29 from MMT, and 27 from M13), and the remaining 40 per cent are objects with photo-z from M13. The multi-wavelength data associated with the X-ray sources are taken from the 2XLSSdOPT catalogue (C13). A matching radius of 6 arcsec (PSF for *XMM*) is used between the X-ray catalogues and the *GALEX*, CFHTLS, SWIRE, and UKIDSS catalogues. Detailed description of the matching criteria and references to the various catalogues can be found in C13.

The L_X in the main sample ranges from $10^{42.1}$ to $10^{45.5}$ erg s^{-1}, with a median of $10^{44.1}$erg s^{-1} (Fig. 2) . The majority (97 per cent) of the main sample has an L_X of 10^{42-45} erg s^{-1}. Half (166, 51 per cent) of the sample have an $L_X \geq 10^{44}$erg s^{-1}; and the rest (158, 49 per cent) are at $10^{42} \leq L_X < 10^{44}$erg s^{-1}, confirming their AGN nature (e.g. Szokoly et al. 2004; Hasinger 2008). There are 46 obscured sources with HR $= 1$, whose reported L_X are lower limits. An effective upper limit is given for these objects, by applying a correction factor of ∼1.7 dex, which is the maximum L_X correction factor found for the rest of the sample. About 60 per cent of the main sample has an HR < -0.2 (X-ray unobscured, e.g. Szokoly et al. 2004). In the spec-z subsample (198/323), 55 per cent (109/198) show broad emission lines (optical type 1). Combining both definitions, overall 65 per cent[5] of the main sample are unobscured (Fig. 1).

For comparison purposes, we retain the small subset of sources outside our preferred redshift range (**supplementary sample**, Table 1) that satisfy the same luminosity and flux requirements, to study the redshift and luminosity dependences. The supplementary sample consists of 20 $z < 0.2$ objects and 12 objects at $2.5 < z < 4.2$.

In addition, since a significant fraction (84 per cent) of the parent sample is not bright in the IR, we extend the IR limit to include fainter sources with 'marginal' detections (**expanded sample**, Table 1). The expanded sample includes 558 AGNs with $L_X \geq 10^{42}$erg s^{-1} in $0.2 < z < 2.5$, but formally undetected: their 250 μm detection significance is between $1 - 3\,\sigma$. The expanded sample will be used to characterize the effects of Malmquist bias commonly present in flux-limited samples.

In Table 1 we summarize the redshift and luminosity distributions for the 3 samples. The basic physical properties including HR, the intrinsic N_H, and the absorption corrected L_X are listed in Table 2. Fig. 2 plots the luminosities, L_X and $L_{IR,\,SF}$ as a function of redshift, colour-coded by the other luminosity. The method to calculate the different IR luminosities is described in Section 3.

2.1 Selection effects

As shown in Fig. 2 (right, inset), IR-bright AGNs in our main and supplementary samples share similar z and L_X distributions as the parent sample of hard X-ray-detected targets (blue dashed line, scaled). This indicates a limited influence on the intrinsic L_X distribution by the level of FIR activity. Similar results have been found in radio AGNs (e.g. 3C samples, Podigachoski et al. 2015), where the far-IR detection rate is unrelated to the radio source type (i.e. orientation).

The redshift distribution, on the other hand, shows a higher fraction of IR-bright AGNs at $0.2 < z < 0.6$ than in the parent sample. This is mainly due to the IR detection requirement, as fainter objects at higher z fall below the relatively shallow detection limit. The sharp drop of the number of objects at $z < 0.2$ is due to the L_X lower limit of $10^{42.0}$ erg s^{-1} and the small volume probed below this redshift, which limit the number of luminous AGNs.

In the main sample, the $z \sim 2$ sources are systematically ∼1–2 dex more luminous in L_X than the $z \sim 0.5$ objects (Fig. 2), due to the flux limit and larger volume probed at high redshift. This increase is broadly consistent with the increase in break luminosity (L_*) in the AGN luminosity function (e.g. Croom et al. 2009; Ranalli et al. 2016; Aird et al. 2015). This indicates that at all redshift in our selected range, we are sampling approximately the same portion of the AGN luminosity function relative to L_*. Similarly, the SFR indicator $L_{IR,\,SF}$ (for definition see Section 3.1) increases by 1–3 dex from $z = 0$ to $z = 2$ (Fig. 2), comparable to the increase in SFR density and in the evolution of the typical ratio of SFR to stellar mass along the star-forming MS (e.g. Speagle et al. 2014). The expanded sample with marginal IR detections – formally undetected, is a continuation of the main sample to lower IR luminosities at all redshifts (crosses, Fig. 2). Inclusion of these 1–3 σ IR undetected sources provides information below the formal flux limit, allowing us to check for systematic effects in the main sample due to Malmquist bias.

[5] ∼15 per cent of the X-ray obscured sources show broad lines (optical type 1).

Table 1. The range of X-ray and IR luminosities in bins of redshift.

Redshift bins	$z \leq 0.2$	$0.2 < z \leq 0.5$	$0.5 < z \leq 1.0$	$1.0 < z \leq 1.5$	$1.5 < z \leq 2.5$	$z > 2.5$	Total
Main sample	...	63 (22 %)	106 (17 %)	88 (14 %)	66 (11 %)	...	323 (14 %)
Expanded sample	...	76 (27 %)	165 (26 %)	156 (24 %)	161 (27 %)	...	558 (23 %)
Supplementary sample	20 (16 %)	...	...	...	...	12 (10 %)	32 (2 %)

Note. In parenthesis are the percentage among the parent sample of 2399 hard X-ray-detected AGNs in the same redshift range.

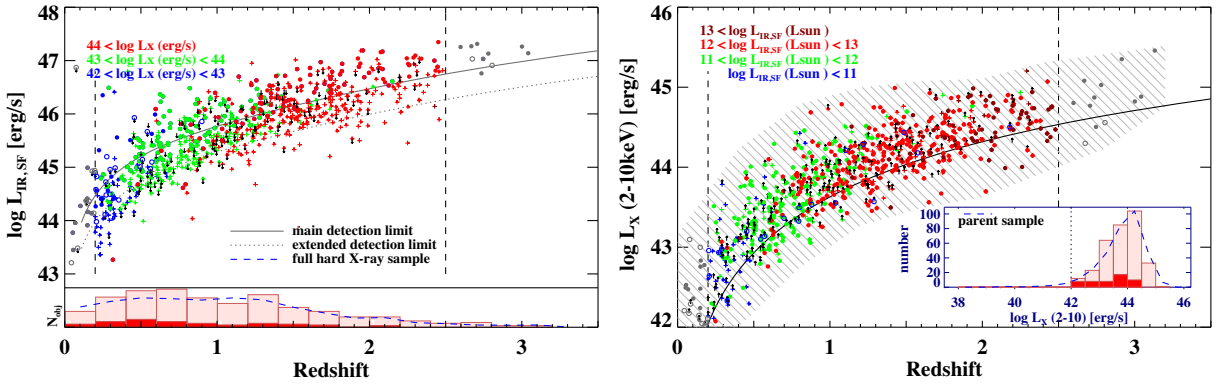

Figure 2. The AGN corrected IR luminosity ($L_{\rm IR,SF}$, left) and the absorption corrected X-ray luminosity ($L_{\rm X}$, right) as a function of redshift. Plotted are the main sample of 323 IR-bright AGNs at $0.2 < z < 2.5$ (coloured dots), the supplementary sample of IR-bright AGNs at $z < 0.2$ and $z > 2.5$ (grey dots), and the expanded sample of IR-undetected AGNs (crosses). The data points are colour coded by the other luminosity, as labelled in the legend. Filled circles mark the unobscured AGNs (X-ray unobscured or optical type 1), which includes 65 per cent of the main sample. Open circles are the obscured AGNs (X-ray obscured and optical type 2). Arrows mark the X-ray obscured sources with an HR > -0.2, which are $L_{\rm IR,\,SF}$ upper limits (left) and $L_{\rm X}$ lower limits (right). The black curves show the 3σ (solid) and $1\,\sigma$ (dotted) detection limits in the FIR (left) and the nominal detection limit in the X-ray (right; Section 2). Data points sometimes fall below the limits because of the AGN correction in the IR (Section 3.1), and the exposure time difference among X-ray pointings (Chiappetti et al. 2013). The left inset shows the redshift distribution of the main sample, and in red is the distribution for targets with $L_{\rm IR,\,SF}$ upper limits. The right inset shows the distribution of the absorption corrected hard X-ray luminosity $L_{\rm X}$ (2–10 keV) of the main sample, and in red is the distribution for targets with X-ray lower limits.

Finally, since both spectroscopic and photometric redshift determination require optical spectra or photometry, the ER distribution is not homogeneous across redshift. At high z, only high ER, luminous targets could be detected. We will discuss this specific selection effect in more detail in Section 3.2 and Section 4.1. These selection effects should be borne in mind when interpreting the results in Section 4.

3 ANALYSIS

3.1 IR luminosity, SFR, and dust mass

In this section, we estimate the total IR and FIR luminosities ($L_{\rm IR}^{8-1000}$, $L_{\rm FIR}^{30-1000}$) based on the rest-frame SEDs for the IR-bright AGNs. The SEDs are constructed from optical through the FIR bands: u^*, g', r', i', z' (CFHTLS); J, H, K (UKIDSS); 3.6, 4.5, 5.8, 8.0 μm (SWIRE-IRAC); 24, 70, 160 μm (SWIRE-MIPS); 250, 350, 500 μm (HerMES). For the Herschel data, the total errors (instrumental + confusion noise) are used in the fitting procedure. We adopt the T$-\alpha-\beta$ model from Blain, Barnard & Chapman (2003), where T is the dust temperature, β is the emissivity index, and α the power-law index. This method fits the SED longwards of 5 μm without any assumptions about the heating source, be it AGN or SF. Instead of a pure modified blackbody (MBB) on both the Rayleigh–Jeans and Wien tails, a power-law function ($f_\nu \propto \nu^{-\alpha} B(\nu, T_{\rm dust})$) is used in the mid-IR (5–10 μm) Wien side to account for contributions from warmer dust. Here, $B(\nu, T_{\rm dust})$ is the blackbody Planck function. SED examples using the same method can be found in Dai et al. (2012). We adopt $\beta = 2.0$ (Priddey et al. 2003) and allow α to vary. This additional term is then matched to the MBB component at a transition point, where the two functions share equal zeroth and first-order derivatives. The transition wavelengths vary from case to case. The corresponding peak dust temperature ranges from 5 to 100 K, with a median around 30 K, similar to normal star-forming galaxies. As a result of the larger errors in the FIR flux, compared to the main and supplementary samples, the expanded sample has a systematically 2–3× larger (∼40–50 per cent) uncertainty in their $L_{\rm IR}$ and $L_{\rm FIR}$ estimates.

Utilizing the X-ray data, we develop a three-step method to decompose the AGN and SF contributions in the FIR regime. Step 1 is to estimate the AGN contribution to the IR luminosity from the X-ray. This correlation is based on the assumption that the X-ray, especially in the hard band, and mid-IR are both dominated by AGN emission. Here, we choose 6 μm to enable extrapolation into the far-IR regime because AGN SEDs may vary significantly longwards of the rest-frame 10 μm for different AGN populations. For instance, in Dai et al. (2012) a variation on the order of 1.5 dex was found between the 250 μm IR-detected and IR-undetected AGNs. Several published relations exist regarding the X-ray to 6 μm correlations for AGNs with $L_{\rm X}$ in the range of 10^{41-46} erg s^{-1}, for both obscured and unobscured populations (e.g. Lutz et al. 2004; Fiore et al. 2009; Gandhi et al. 2009; Lanzuisi et al. 2009; Mateos et al. 2015; Stern 2015; Chen et al. 2017). In this work, we adopt the results from Stern (2015):

$$\log {\rm L}(2-10\,{\rm keV}) = 40.981 + 1.024{\rm x} - 0.047{\rm x}^2, \quad (1)$$

MNRAS 478, 4238–4254 (2018)

Table 2. Derived properties for IR-bright AGNs.

Xcatname	redshift	zflag	T_{dust} (K)	α	HR	N_H (int) (cm^{-2})	L_X ($erg\,s^{-1}$)	$L_{IR,\,AGN}$ ($erg\,s^{-1}$)	$L_{IR,\,SF}$ ($erg\,s^{-1}$)	SFR ($M_\odot\,yr^{-1}$)	logM_{dust} ($M_\odot$)	log$M_\bullet$ ($M_\odot$)	flag
(1)	(2)	(3)	(4)	(5)	(6)	(7)	(8)	(9)	(10)	(11)	(12)	(13)	(14)
2XLSSd J021324.6-033512	1.142	1	47.6 ± 7.3	2.0 ± 0.0	-0.06	2.8e+22	44.64	45.9 ± 0.7	46.7 ± 1.0	2110	8.5 ± 1.3	9.4	1
2XLSSd J021407.8-035309	0.987	1	18.7 ± 1.7	0.4 ± 0.0	0.28	5.8e+22	44.13	45.1 ± 0.6	46.4 ± 1.0	1100	9.2 ± 1.1	8.5	1
2XLSSd J021418.7-033934	1.136	2	20.4 ± 0.9	1.4 ± 0.0	-0.08	2.6e+22	44.24	45.3 ± 0.6	46.2 ± 1.0	730	9.4 ± 1.3	...	1
2XLSSd J021434.2-035553	1.426	1	51.9 ± 1.3	3.0 ± 0.1	-0.48	7.7e+20	45.14	46.8 ± 0.8	0	0	8.3 ± 0.9	8.6	1
2XLSSd J021451.6-035339	0.614	1	29.1 ± 5.2	2.4 ± 0.2	-0.52	0.0	43.18	43.8 ± 0.5	45.6 ± 0.9	160	8.3 ± 1.2	...	1

Notes. (1) Object identification same as in Chiappetti et al. (2013). (2) Redshift of the object. (3) Redshift flag, 1 for spec-z, 2 for photo-z. (4) and (5) Peak dust temperature and power-law index derived from SED fitting as described in Section 3.1. (6) X-ray Hardness ratio [HR $= (H - S)/(H + S)$] based on net count rates. (7) Intrinsic column density derived from redshift and HR as described in Section 2. If the object is only detected in the hard X-ray, a lower limit of 1.00e+23+ is assigned. If the object has an HR <-0.5, no N_H correction was made and a value of '0' was assigned. (8) Obscuration corrected rest-frame X-ray luminosity (2–10 keV). (9) AGN contributed IR luminosity (8–1000 μm), based on X-ray luminosity converted 6 μm luminosity (Stern 2015) and SED template from (Dai et al. 2012). (10) AGN-subtracted IR luminosity (8–1000 μm). A value of '0' marks purely AGN-driven IR luminosity. (11) SFR derived from (10) using the Kennicutt (1998) relation. A value of '0' marks purely AGN-driven IR luminosity. (12) Dust mass derived from FIR photometry as described in Section 3.1. (13) SMBH mass derived for the subsample with optical broad emission lines as described in Section 3.2. (14) Sample flag, 1 for main sample, 2 for expanded sample, and 3 for supplementary sample. This table is available in its entirety with a machine-readable form in the online journal.

where $L(2\text{–}10\,\mathrm{keV})$ is in units of erg s^{-1}, and $x = \log(\nu L_\nu(6\mu\,\mathrm{m})/10^{41}\mathrm{erg\,s^{-1}})$. This relation is consistent with earlier work at the fainter end and covers a wide range of $L_X = 10^{42-46}$ erg s^{-1}, which overlaps with the luminosity range of our sample.

In step 2, we convert the X-ray-based 6 μm luminosity (L_6) to the AGN IR ($L_{\mathrm{IR,\,AGN}}$) and bolometric luminosities (L_{AGN}) using an AGN template that extends to rest-frame 1000 μm (Dai et al. 2012, D12). The D12 mean SED template is chosen because it was constructed with detailed FIR SED information with SPIRE detections and stacks of FIR-undetected AGNs,[6] while earlier works, e.g. Richards et al. (2006, R06), Netzer et al. (2007, N07), Mullaney et al. (2011, M11) stopped or extrapolated beyond rest-frame 100 μm where no data were available. Since the AGN contribution to the rest-frame FIR is an unsettled question with a large variation (≥1 dex), in this study we adopt the D12 mean SED based on the stacks of ∼300 SPIRE-undetected AGNs. This is likely an underestimate for the small subsample of AGN-starbursts (∼10 per cent of all quasars according to D12), whose L_{IR} and L_{FIR} are 0.3–0.4 dex higher. Given the redshift range used to construct the mean SED, the intrinsic uncertainty of this template increases from ∼0.3 dex to >1 dex beyond 100 μm. Compared to the extrapolation of the above mentioned templates [R06, N07, M11, and Dale et al. (2014, D14)], the conversion factors between L_6 and L_{IR} are always consistent within 0.2 dex. However, between L_6 and L_{FIR}, the deviation is larger and varies from −0.06 (M11), 0.42 (R06), 0.47 (D14), to 0.53 (N07) dex, respectively. Regardless, these differences are 10 times smaller than the intrinsic scatter (covering 90 per cent of the sample) of a few dex and can be considered consistent with each other. In summary, factors of 0.9 and 2.5 were used to convert $L_{6,\mathrm{AGN}}$ to $L_{\mathrm{FIR,AGN}}$ and $L_{\mathrm{IR,AGN}}$, respectively; and a factor of 8.0 was used to convert the L_X-based L_6 to the AGN bolometric luminosity L_{AGN}.

In the last step (step 3), we subtract $L_{\mathrm{IR,AGN}}$ and $L_{\mathrm{FIR,AGN}}$ from the observed L_{IR} and L_{FIR} derived from SED fitting, and estimat the SFR based on the AGN-corrected $L_{\mathrm{IR,SF}}$ and $L_{\mathrm{FIR,SF}}$ using the Kennicutt relation (Kennicutt 1998).[7] Fig. 3 shows the distribution of AGN contribution to the IR (FIR) in the main and expanded samples. The average AGN contribution to the total IR luminosity (red) is at least 11 per cent in the main sample. The actual percentage is higher than quoted here, as L_X in ∼15 per cent of the main sample are lower limits. More than ∼8 per cent has an AGN-dominated L_{IR}, resulting in a > 50 per cent drop in the SFR, and 4 per cent has a purely AGN-heated L_{IR} (i.e. $L_{\mathrm{IR,AGN}} > L_{\mathrm{IR}}$, or SFR = 0). As a result of the scatter in the $L_X - L_{6,\mathrm{AGN}}$ relation, the uncertainties in $L_{\mathrm{IR,SF}}$ and SFR are also higher for objects with an AGN-dominated IR. On the other hand, for FIR luminosities (blue histograms in Fig. 3), the AGN contribution is lower, with an average value of at least 6 per cent, and only ∼1 per cent has an AGN-dominated FIR. The reason that L_{FIR} has a smaller fraction of purely AGN-heated sources than L_{IR} is because of the different conversions from $L_{6,\mathrm{AGN}}$ to $L_{\mathrm{IR,AGN}}$ and $L_{\mathrm{FIR,AGN}}$. These uniform, template-based conversions are subtracted from the observed SEDs, which differ from the template on an individual basis. As a result, the AGN subtracted $L_{\mathrm{IR,SF}}$ and $L_{\mathrm{FIR,SF}}$ values are not always correlated. For the expanded sample with lower IR luminosity, the fractional AGN contribution to the IR luminosities is higher, as expected given the constant X-ray flux limit (Fig. 3, inset). The average AGN contribution is at least 23 per cent in the IR, and 26 per cent of the expanded sample has an AGN-dominated IR (>50 per cent drop in the SFR), and 11 per cent has purely AGN-heated L_{IR} (SFR = 0). For L_{FIR}, AGN contribution has an average of 13 per cent, and 4 per cent of the expanded sample has an AGN-dominated FIR.

These high values of correction factor demonstrate the importance of IR AGN/SF decomposition for SFR estimates. It is worth noting that the average AGN fraction in the IR increases with redshift. This is a known selection effect due to converting the observed 250 μm to the rest-frame with a fixed, and steep, SED template. This results in the inclusion of galaxies with relatively lower L_{FIR} at similar L_X, as the observed frame approaches the IR SED peak.

We compare the AGN-removed $L_{\mathrm{IR,SF}}$ to the total L_{FIR} and find that they are consistent within errors for 92 per cent of the main sample. Therefore, we suggest that when AGN decomposition is not possible, $L_{\mathrm{FIR}}(30-1000\,\mu\mathrm{m})$ can be used as a convenient proxy for the AGN-removed $L_{\mathrm{IR,SF}}$. As a check, we also subtract the average contribution to L_X from SF using the SFR–L_X relation (Ranalli, Comastri & Setti 2003), and confirm that L_X is dominated by the AGN: the non-AGN contribution to L_X is <2 per cent in all chosen redshift and luminosity bins.

We then estimate the dust mass (M_{dust}) of the sample using the following formula (Beelen et al. 2006):

$$M_{\mathrm{dust}} = \frac{S_{\nu 0} D_{\mathrm{L}}^2}{(1+z) k_{\mathrm{d}}(\nu) B(\nu, T_{\mathrm{dust}})}, \quad (2)$$

where $k_{\mathrm{d}}(\nu) = k_0(\nu/\nu_0)^\beta$ is the dust absorption coefficient, T_{dust} and B are the dust temperature and the black body Planck function, and D_{L} is the luminosity distance based on redshift. Here, we use the flux at 250 μm S_{250}, and k_{d} from Alton et al. (2004). The majority (86 per cent) of the sample has $\log M_{\mathrm{dust}} > 10^8\,\mathrm{M_\odot}$ (99 per cent at $> 10^7\,\mathrm{M_\odot}$) similar to the dust-rich quasars detected in the FIR and (sub)mm (e.g. Dai et al. 2012). This value is ∼1–2 dex higher than the dust mass estimated for the local Palomar-Green (PG) quasars, confirming that this IR-bright AGN sample is dominated by objects with ample dust, likely in the process of actively forming stars. Table 2 lists the derived properties of the sources for the IR-bright AGN samples (main, supplementary, and expanded). The full table is available in a machine-readable form of the online journal.

3.2 SMBH mass, eddington ratios, and BHAR

About 90 per cent of the optical type 1 (broad-emission line) AGNs in the main sample (i.e. 34 per cent of the full main sample) have a spectrum of sufficiently high signal-to-noise to derive reliable virial SMBH masses ($\mathrm{M_\bullet}$). Note that the AGN luminosities for targets detected only in the X-ray hard band are lower limits. The virial SMBH masses are commonly expressed as (e.g. Dai et al. 2014):

$$\log\left(\frac{\mathrm{M_\bullet}}{\mathrm{M_\odot}}\right) = a + b\log\left(\frac{\lambda L_\lambda}{10^{44}\mathrm{erg\,s^{-1}}}\right) + c\log\left(\frac{\mathrm{FWHM}}{\mathrm{km\,s^{-1}}}\right) \quad (3)$$

where $\mathrm{M_\odot}$ is the solar mass, FWHM is the full width at half-maximum of the emission line profile, and λL_λ is the continuum luminosity at 5100 Å (Hβ, Hα), 3000 Å (MgII), and 1350 Å (CIV), respectively. The term λL_λ is used as a proxy for the radius of the broad line region (Kaspi et al. 2000; Bentz et al. 2013). The coefficients a and b are empirical values based on SMBH masses determined via the reverberation mapping method, and c normally

[6] https://app.box.com/v/dai12-templates

[7] Note the definition of FIR in Kennicutt (1998) equals the total IR (8–1000 μm). In this work, IR and FIR refer to ranges (8–1000 μm) and (30–1000 μm), respectively.

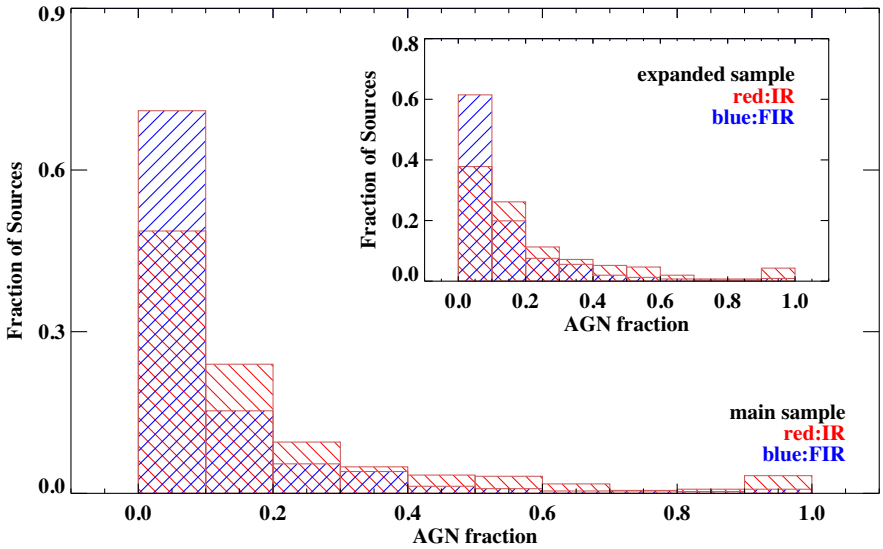

Figure 3. The distribution of the fractional AGN contribution to the total IR (red) and FIR (blue) luminosities for the main sample and the expanded sample (inset). The *x*-axis shows the $f_{\rm AGN}$ (i.e. $L_{\rm (F)IR,AGN}/L_{\rm (F)IR,obs}$), and the *y*-axis marks the frequency of a certain $f_{\rm AGN}$. For the main sample, AGN contributes an average of >11 per cent and 6 per cent to $L_{\rm IR}$ and $L_{\rm FIR}$, respectively. The actual percentage is higher than quoted here, since $L_{\rm X}$ in ∼15 per cent of the main sample are lower limits. In about 4 per cent (1 per cent) of the IR-bright AGN main sample, the IR (FIR) luminosity is purely AGN-heated (i.e. $L_{\rm (F)IR,AGN} \geq L_{\rm (F)IR,obs}$, thus SFR = 0). The reason for a smaller fraction of purely AGN-heated $L_{\rm FIR}$ than $L_{\rm IR}$ is due to the AGN subtraction from the 'observed' $L_{\rm IR}$ and $L_{\rm FIR}$. For the expanded sample, the average AGN contribution is at least 23 per cent (13 per cent) in the IR (FIR), and 11 per cent (4 per cent) has a purely AGN-heated IR (FIR) luminosity.

has a fixed value of 2 (e.g. Vestergaard & Peterson 2006), which exemplifies the virial nature of the broad-line region ($M_\bullet \propto Gv^2R^{-1}$). Here, we use the FWHM (in $\rm kms^{-1}$) of the continuum subtracted emission line as the line width proxy. We adopt the IDL line fitting procedures from Dai et al. (2014, section 3) for C IV (0.660, 0.53, 2.0), Mg II (0.740, 0.62, 2.0), Hβ (0.672, 0.61, 2.0), and Hα (0.522, 0.64, 2.06) lines; in brackets are the parameter sets (a, b, c) from Vestergaard & Peterson (2006); Shen et al. (2011); McLure & Dunlop (2004); Greene & Ho (2005), respectively.

For the subsample with spectra showing broad-emission lines of sufficient quality, we use the $M_\bullet$ and $L_{\rm AGN}$ calculated in Section 3.1, and compare the ER ($L_{\rm AGN}/L_{\rm edd}$) in four fiducial redshift bins (Fig. 4), where $L_{\rm edd}/{\rm erg\ s^{-1}} = 1.3 \times 10^{38}(M_\bullet/M_\odot)$. The median ER shows a general increase from low z to high z. At high z, low-mass AGNs are generally not detectable unless the ERs are sufficiently high that $L_{\rm X}$ is above the detection limit. This ER selection effect is less prominent at $z < 1.5$, where the ER distribution shows a wide range and scatters into the ER < 0.01 region. Whereas from z= 0.5–1.5, more luminous AGNs are being selected, the data points are distributed along constant ERs, indicating systems of similar accretion conditions.

We also calculate the BHAR($\dot{M}_\bullet$) using the hard $L_{\rm X}$ as a proxy

$$\frac{\rm BHAR}{\rm M_\odot\ yr^{-1}} = 0.15\frac{0.1}{\epsilon}\frac{kL_{\rm X}}{10^{45}{\rm erg\ s^{-1}}}, \quad (4)$$

where ϵ is the mass-energy conversion efficiency, and k is the conversion factor between $L_{\rm X}$ and the AGN bolometric luminosity. Here, we adopt k = 22.4 from Vasudevan & Fabian (2007, based on local AGNs), and a typical ϵ value of 0.1 (Marconi et al. 2004), meaning that about 10 per cent of the mass is converted into radiative energy. These values are chosen to allow direct comparisons with other studies involving $\dot{M}_\bullet$ estimates (e.g. Mullaney et al. 2012b; Chen et al. 2013).

4 RESULTS AND DISCUSSION

4.1 Correlation between AGN activity and star formation

In Fig. 5, we compare the $L_{\rm AGN}$–$L_{\rm IR,SF}$ relation of the main sample to literature results. Individual objects are plotted as grey dots (X-ray unobscured or optical type 1) or open circles (X-ray obscured and optical type 2). The $L_{\rm X}$ lower limits and accordingly, $L_{\rm IR,SF}$ upper limits of the HR = 1 sources are marked by arrows. The thick black dash-dotted line shows the best-fitting correlation for the main sample, with a power law of $L_{\rm IR,SF} \propto L_{\rm AGN}{}^{(0.62\pm0.05)}$ and a high significance (P< 0.0001). We note that, since our sample is flux limited, the effective IR luminosity limit is higher at higher redshift. Thus, the fainter end of the IR-bright AGN population is missed especially at high z, also increasing the average $L_{\rm IR}$ (Fig. 2). We will probe this fainter population later using the combined sample (main + expanded, See Sections 4.2 and 4.4).

Our best-fitting correlation agrees well with the Xu et al. (2015a, X15) result (dashed orange line), which shares almost identical selection criteria, except an additional selection using the MIPS 24 μ m flux. The 24 μm flux selection is highly complete for AGN populations (Krawczyk et al. 2013; Dai et al. 2014), as is further demonstrated by the similar correlations found between X15 and this work. Our correlation is also in general agreement with Chen et al. (2013, light green stars in Fig. 5), after taking the scatter and binning methods into account.

The steeper Azadi et al. (2015) results were based on data binned by $L_{\rm IR}$ (see also Section 4.3). The Hickox et al. (2014) model (grey-shaded area) underpredicts the $L_{\rm IR,SF}$ for the most luminous IR-bright AGNs in our sample. This model flattens at lower luminosities after accounting for the effects of short-term AGN variability. The disagreement between this work and Chen et al. (2015, C15) can be explained by the different sample compositions. C15 includes a high fraction of type 2 AGNs (brown stars) as well as stacks of

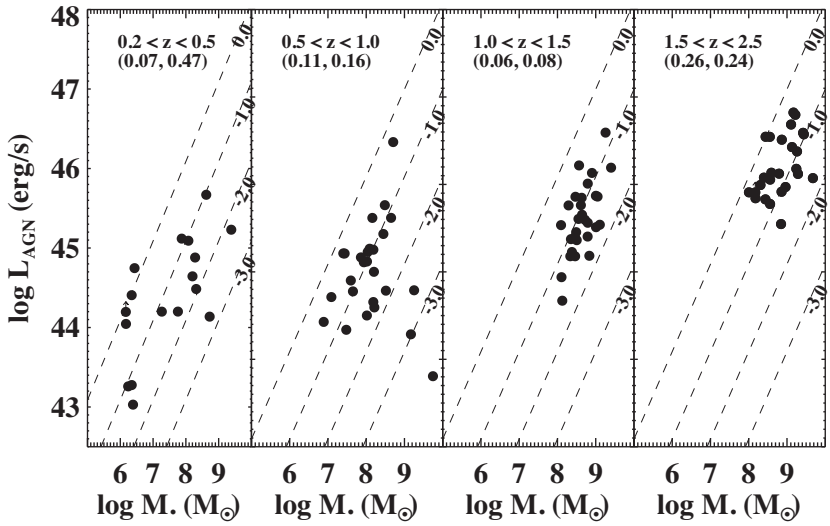

Figure 4. The AGN bolometric luminosity versus SMBH mass ($M_\bullet$) for the subsample of IR-bright AGNs with reliable BH mass estimates (∼34 per cent of the main sample). Dashed lines mark the Eddington ratios (ERs) at 1, 0.1, 0.01, and 0.001, and are labelled by log (ER). At $z < 1.0$, the IR-bright AGN sample has a wide range of ER: $0.001 < \mathrm{ER} < 0.01$, whereas at high z, the sample is limited to massive, $\mathrm{ER} > 0.01$ AGNs. In brackets are the median and standard deviation of the ER in each redshift bin.

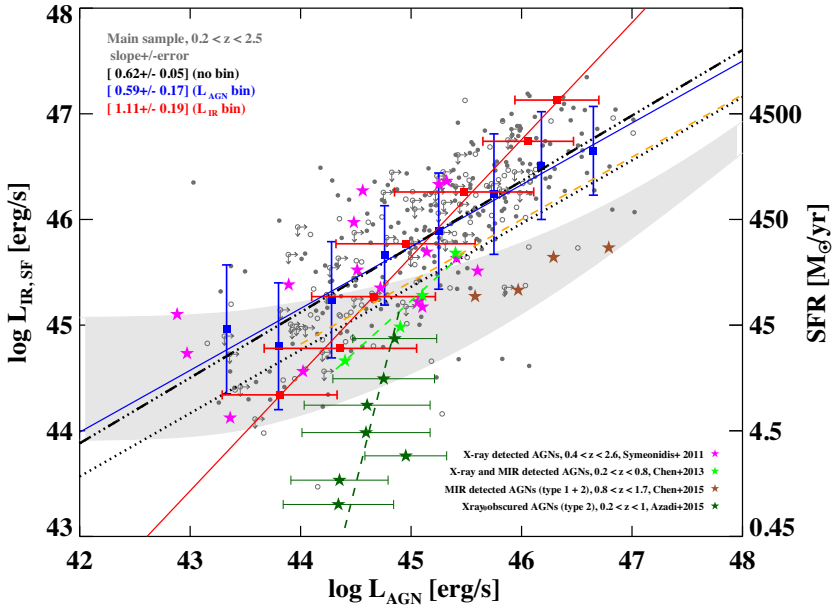

Figure 5. Correlation between L_{AGN} and $L_{\mathrm{IR,SF}}$ for the main sample. Individual IR-bright AGNs are plotted as open- and filled-grey circles, same as in Fig. 2. The best-fitting correlation (without binning) is marked by the dash-dotted black line, and the same relation for the main + expanded + supplementary sample by the dotted black line. In blue is the average L_{AGN} plotted in bins of $L_{\mathrm{IR,SF}}$, in red is the average $L_{\mathrm{IR,SF}}$ plotted in bins of L_{AGN}. The shaded region marks the Hickox et al. (2014) model at $0.01 < z < 3.5$. Also plotted are the binned data of IR-bright AGNs from the literature: pink stars are the X-ray- and FIR-detected AGNs from Symeonidis et al. (2011), green and brown stars are the X-ray- and mid-IR-detected AGNs from Chen et al. (2013, 2015), the dark green stars are the X-ray-obscured AGNs from Azadi et al. (2015). Dashed coloured lines mark the literature correlations in Chen et al. (2013) (light green), Azadi et al. (2015) (dark green), and Xu et al. (2015a) (orange), respectively. Our results are in good agreement with Xu et al. (2015a), and in general agreement with Chen et al. (2013). The selection effects and caveats are discussed in Section 4.

FIR-undetected objects, thus their averaged values occupy a lower IR region than our correlation.

Another cause of the observed differences between our sample and some literature results is the use of different SFR estimators. In Fig. 5, the 15 AGN-ULIRG/LIRG systems from Symeonidis et al. (2011) are systematically higher in L_{IR} than our sample (with a ∼0.2 dex IR offset at similar L_{AGN}). This is because the SED library used there, Siebenmorgen & Krügel (2007), was based on pure star-forming galaxies. As demonstrated earlier, the AGN contribution to L_{IR} and L_{FIR}, though small (with an average of 23 per cent and 11 per cent), is not negligible. If we correct the L_{IR} by applying the empirical L_{IR}-to-L_{FIR} correction in our sample and use L_{FIR} as a proxy for $L_{\mathrm{IR,SF}}$ (See Section 3.1), the Symeonidis et al. (2011) data agree better – the offset drops to ∼0.05 dex. Careful treatment

of AGN removal is needed when attributing higher L_{IR} to enhanced SF in the AGN-host system.

The different SED models also bias the SFR estimates. For instance, Azadi et al. (2015) utilized the iSEDfit code (Moustakas et al. 2013), which was based on the UV and optical photometry. This code accounts only for unobscured SF with no AGN removal. It yields systematically lower SFR estimates than using *Herschel* FIR data (Azadi et al. 2015; Section 4.3), as dust-reprocessed (IR) extinction was not included. This explains their systematically lower values in Fig. 5 (dark green stars).

Several earlier studies used a single band rest-frame FIR photometric measurement as the proxy for SF. Since there is a non-negligible AGN contribution to the IR, especially at $\lambda < 30\,\mu$m, as demonstrated in Section 3.1, this approach may overestimate the SFR. Besides the L_{IR} and L_{FIR} defined earlier, to test this at longer wavelength, we estimate the integrated luminosities at $L_{60-1000}$ and $L_{100-1000}$, based the same SED fitting procedure used in Section 3.1. We find an average AGN contribution of ∼7 per cent in both luminosities. If interpolated to single bands, the AGN contribution to L_{60} and L_{100} is ∼2 per cent, almost negligible. The higher AGN contributions to integrated values than at single bands are due to the D12 AGN SED template being flatter towards longer wavelengths ($\lambda > 100$ μm). Note that in our case any monochromatic luminosity is interpolated from the SED fit and so is not independent from the integrated values. Actual AGN contributions may vary case by case at these wavelengths.

Since Fig. 5 is plotted in luminosity space, it is important to separate any real correlation from effects resulting from the presence of redshift on both axes. The flatter than linear (1:1), $\alpha \sim 0.6$ slope in Fig. 5 indicates a true AGN–SF correlation, but is also affected by a number of factors, such as the increasing AGN fraction with redshift (see Section 3.1), and the X-ray absorption correction, which broadens the range of L_X. To test the validity of this correlation, we first compare the fit results across our various samples, as discussed below. Then, in Section 4.2, we use the partial correlation technique to examine the correlation between different parameters. We will explore the binning effects in Section 4.3.

Combining the main and expanded samples significantly increases, sometimes doubles, the IR luminosity parameter space at any given redshift. Fitting the combined sample results in a consistent slope of 0.60 ± 0.03 (dotted black line in Fig. 5), with a lower normalization factor, agreeing better with the Chen et al. (2015) results. Similarly, including the supplementary sample at the low and high z ends results in a wider redshift range ($0.04 < z < 4.2$), but the slope remains consistent at 0.63 ± 0.04. The consistency of slopes estimated from fitting various subsamples confirms that the observed correlation is not purely caused by the Malmquist bias. To further test the effect of flux limits on the observed correlation, we artificially increase the flux limits by factors of 5, 7, 9, and 11. Consistent slopes and normalization factors are found, with slope values at 0.60 ± 0.07, 0.51 ± 0.11, 0.59 ± 0.18, and 0.58 ± 0.23, respectively. This confirms that the observed trend is intrinsic and not caused by the IR flux limit of the sample.

For the subsample of broad-emission line AGNs with a reliable $M_\bullet$ estimate, we also check the effects of ER and $M_\bullet$ on the L_{AGN}–SFR relation by binning the data by accretion efficiencies. Positive linear correlations are confirmed, although the smaller subsamples do not provide meaningful constraints on the slopes. We conclude that neither the mass nor the ER of the SMBH regulates the AGN–SF correlation significantly, at least not on a time-scale short enough to affect the observed SF.

Table 3. Bivariate correlation analysis for the main sample.

Correlation	Probability	Correlation	Probability
L_X versus $L_{IR,SF}$	<0.0001	L_X versus $L_{FIR,SF}$	<0.0001
L_X versus L_{IR}	<0.0001	L_X versus L_{FIR}	<0.0001
L_X versus L_{60}	<0.0001	L_X versus L_{100}	<0.0001
F_X versus F_{60}	0.5980	F_X versus F_{100}	0.2324

Table 4. Bivariate correlation analysis for the combined (main + expanded + supplementary) sample.

Correlation	Probability	Correlation	Probability
L_X versus $L_{IR,SF}$	<0.0001	L_X versus $L_{FIR,\,SF}$	<0.0001
L_X versus L_{IR}	<0.0001	L_X versus L_{FIR}	<0.0001
L_X versus L_{60}	<0.0001	L_X versus L_{100}	<0.0001
F_X versus F_{60}	0.0106	F_X versus F_{100}	0.0073

4.2 Correlation analysis

We then test for the presence and significance of correlations between the fluxes and luminosities at various wavelengths across the SED. Luminosity versus luminosity correlations are a challenge to assess since both parameters depend on the redshift to derive the L values from the observed fluxes. Besides, both flux and luminosity correlations can be strongly affected by selection effects for a given sample. In this section, we take advantage of our large, well-defined sample to test the interrelationships between these variables, with an emphasis on assessing the correlation significance independent of redshift.

Tables 3 and 4 summarize the results of the bivariate correlation analysis for the main and the combined samples, respectively. We test the correlations between L_X versus L_{60}, L_X versus L_{100}, L_X versus L_{IR}, L_X versus L_{FIR}, L_X versus $L_{IR,\,SF}$ and L versus $L_{xFIR,SF}$, where L_{60} and L_{100} are the luminosities at 60 and 100 μm, calculated from the SED fitting. A correlation is considered significant if the probability (P) of occurring by chance is $P < 0.01$. We find positive and significant bivariate correlations between the AGN (L_X) and all IR luminosities. However, in the main sample there is no bivariate correlation between the rest-frame fluxes (F_X versus F_{60} or F_X versus F_{100}; Tables 3 and 4), suggesting that their observed, strong AGN–IR luminosity correlations are primarily redshift driven. Adding sources below the flux limit in the combined sample probes the fainter IR population, and includes information on the luminosity distribution by retaining the individual estimates for each source. Bivariate correlation analysis reveals a marginal correlation for F_X versus F_{60} ($P = 0.0106$) and a significant correlation for F_X versus F_{100} ($P = 0.0073$), suggesting that a residual AGN–SF correlation may be present.

We next perform partial Spearman rank analysis (PSRA, e.g. Kendall & Stuart 1976; Isobe, Feigelson & Nelson 1986; Akritas & Siebert 1996) between the AGN and IR properties. PSRA allows for a correlation analysis in the general multivariate case, and tests for correlations between subsamples of parameters while holding constant all other variables in the matrix. In particular, these tests allow us to investigate correlations independent of the, otherwise

Table 5. Partial correlation analysis.

Correlation	Main sample		Combined sample	
	P	*r*	*P*	*r*
L_X versus L_{60}	0.377	0.018	<0.005	0.218
F_X versus F_{60}	0.382	− 0.017	<0.005	0.267
L_X versus L_{100}	0.388	0.016	<0.005	0.152
F_X versus F_{100}	>0.400	0.011	<0.005	0.205
L_X versus L_{IR}	<0.005	0.163	0.011	0.129
L_X versus L_{FIR}	0.032	0.105	0.061	0.088
L_{AGN} versus $L_{IR,SF}$	0.297	0.030	>0.400	− 0.014
L_{AGN} versus $L_{FIR,SF}$	0.087	0.070	>0.400	− 0.007

Notes. *P* is the partial Spearman rank probability and *r* the partial correlation coefficient for a correlation between the listed parameters occurring by chance, given that both variables depend on redshift. Partial correlations between all luminosities and redshift are universally significant ($P < 0.005$). Combined sample includes the main, expanded, and supplementary samples.

dominant, effect of redshift. To account for lower limits in our data,[8] we use the survival analysis package ASURV (Lavalley, Isobe & Feigelson 1992) to calculate the bivariate Spearman ranks that are then input to PSRA.

All luminosities (L_X, L_{IR}, L_{FIR}, L_{60}, L_{100}) are found to be primarily and significantly correlated with redshift ($P < 0.005$, not listed in the table). The partial correlation probabilities between pairs of luminosities and fluxes are given in Table 5. No significant correlations are found in the main sample after removing the redshift effect, except for L_X versus L_{IR}. However, for the combined sample, significant correlations are present in F_X versus F_{100} and L_X versus L_{100}, as well as in F_X versus F_{60} and L_X versus L_{60}. The partial correlations between L_X and the broad-band IR luminosities (L_{IR}, L_{FIR}), are marginally significant ($P = 0.011$, $P = 0.061$, respectively). Since our primary motivation is to determine whether or not there is a correlation between SF and AGN, we also test the partial correlation between $L_{IR,SF}$ versus L_{AGN}. However, this correlation is not significant.

Considering the results of all these correlations, along with the relatively low AGN contribution at these single bands (∼2 per cent, Section 4.1), we used L_{60} and L_{100}, interpolated from the SEDs, as reliable proxies for the SFR. The significant partial correlations between L_X versus L_{100} and F_X versus F_{100} thus suggest an AGN–SF connection, which remains significant after accounting for redshift dependence. The lack of correlation between $L_{IR,SF}$ and L_{AGN} is consistent with this conclusion if the uncertainties and increased dispersion arising from the AGN subtraction process masks any real correlation, as suggested by simulation results (Gabor & Bournaud 2013; Hickox et al. 2014; Volonteri et al. 2015a). The main uncertainties in this sample include: L_X obscuration correction (typically ∼0.6 dex, up to 1.7 dex for the ∼14 per cent, HR = 1 sources, Section 2); L_{AGN} estimate (typically ∼ 0.3 dex, up to 0.5 dex, due to the L_X–L_6–L_{AGN} conversion, and is AGN template dependent, Section 3.1); $L_{IR,SF}$ and thus the SFR estimate (typically ∼0.3–0.4 dex, up to >1 dex for outliers from the SED template, Section 3.1). After removing the redshift effect, our sample shows a slope of ∼0.1–0.3 (see next paragraph), which translates to an IR luminosity increase of ∼0.4–1.2 dex over the L_{AGN} span of ∼4 dex in our sample. The typical combined error for L_X + SFR is ∼0.9 dex (∼1.2 if L_{AGN} is used), but for the extreme outliers (<3 per cent), it can reach an order of ∼2–3 dex. If combined with the intrinsic scatter, this typical error is comparable to, and thus sufficiently large to mask out the underlying intrinsic correlation.

An alternative method of removing the strong redshift effect in the bivariate correlations is to test for a correlation over a smaller range of redshift. We compare the least square linear fit between L_{AGN} and $L_{IR,SF}$ for four subsamples with redshift ranges: $0.2 < z < 0.5$, $0.5 < z < 1.0$, $1.0 < z < 1.5$, and $1.5 < z < 2.5$. Over the full redshift range, there is a strong overall bivariate L–$L_{X\,IR,SF}$ correlation ($P < 0.0001$, Section 4.1). For the main sample, within these smaller, subsamples we find significant correlations in the intermediate redshift bins ($P = 0.32$, 0.006, 0.007, and 0.016, z from low to high, no binning), suggesting a weak ($\alpha \sim 0.2$) underlying AGN–SF relation. Similar to the partial analysis results, using the combined sample (main + expanded) the correlations are more significant ($P = 1e{-}5$, $4e{-}5$, 0.102, 0.0057, z from low to high), again showing a flatter slope ($\alpha \sim 0.2$, Fig. 6) in each subsample than in the redshift-driven, overall correlation. The exception is the subsample with redshift range $1.0 < z < 1.5$, which shows a larger scatter. Our result agrees well with Netzer (2009), where an overall bivariate linear correlation with similar slope was reported, and is consistent with Stanley et al. (2015), in which using average IR luminosities, including treatment of undetected sources, flat correlations were observed in similar redshift bins.

The effect of different variability time-scales for AGN and SF activity has been studied on a quantitative base via hydrodynamic simulations (e.g. Gabor & Bournaud 2013; Thacker et al. 2014; Volonteri et al. 2015a; McAlpine et al. 2017) and through analytical models (e.g. Hickox et al. 2014). These studies have confirmed that different variability time-scales can result in the observed flat trend in SFR as a function of AGN luminosity. A flat slope does not rule out an underlying strong correlation, given the large scatter introduced by the IR AGN/SF degeneracy and the short time-scale AGN variability. On the other hand, we do not see enhanced SFR towards higher AGN luminosity ($L_X > 10^{44.8}$ erg s^{-1}), as was reported in Rosario et al. (2012), nor suppressed SFR towards luminous AGNs (the 'feedback' effect). Note that 'feedback' can occur at different time-scales (e.g. Fabian 2012; Gabor & Bournaud 2013; Heckman & Best 2014; Hopkins et al. 2016), for instance, mechanical 'feedback' from relativistic jets could occur in 0.1 Myr scale, local 'feedback' of the molecular cloud's dynamical evolution may take ∼1–10 Myr, while galaxy-wide 'feedback', associated with gas cooling, may last much longer.

Based on our bivariate and PSRA results, as well as the correlation significance in the redshift limited subsamples, we conclude that there is a weak (flat, $\alpha \sim 0.2$) but significant relation between SF and the luminosity of the central AGN. After adding the expanded sample the correlations become more significant. Since the correlation is positive, we see no evidence for the quenching of SF by the AGN. However, we cannot exclude the possibility that the feedback process either (1) has significantly different time-scales than the gas-depletion time in these IR-bright AGNs (depends on the exact SFR and gas reservoir, thus could vary from a few Myr to a few 100 Myr), or (2) introduces scatter that masks the underlying correlation.

4.3 The effect of binning on the AGN–SF correlation

Given the rapid and significant variability of many AGNs, e.g. their flux can vary by 100 times in 0.1 Myr (Keel et al. 2012), it

[8] Absorption corrected X-ray flux and luminosity with HR = 1 were treated as lower limits.

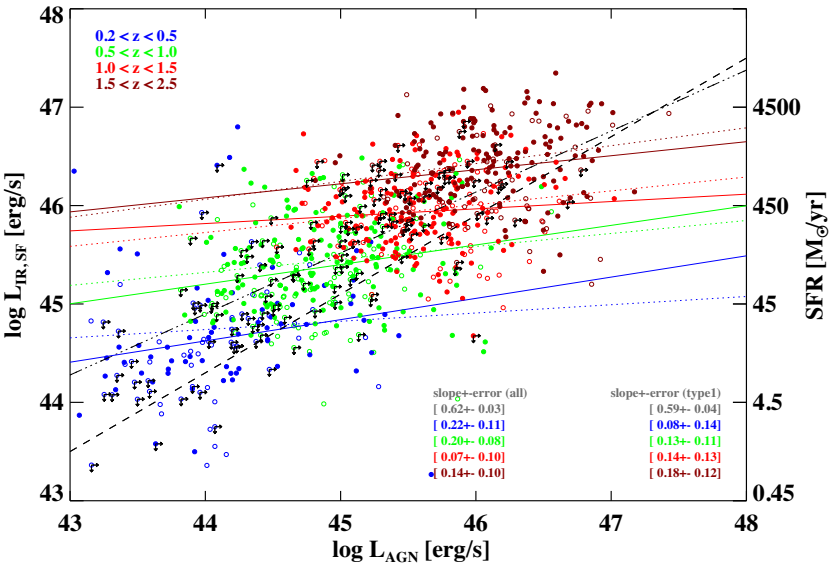

Figure 6. Correlation between $L_{\rm AGN}$ and the AGN removed $L_{\rm IR,SF}$ for the main+expanded sample, colour coded by redshift. The filled (open) circles are the same as in Fig. 2. Objects detected in the hard band only (X-ray lower limits) are marked with arrows. The dash-dotted line is the correlation for the main sample without binning (See Fig. 5). The solid lines are the linear fits to the data in each redshift bin, and the dotted lines are the fits for type 1 AGNs. The dashed line marks the normalized Netzer (2009) relation implied from local type 2 AGNs, with a slope of 0.8. Significant correlations with flatter slopes are observed between $L_{\rm AGN}$ and $L_{\rm IR,SF}$ in the limited redshift subsamples.

Table 6. Derived average properties in each luminosity bin for the main sample.

luminosity range (1)	$N_{\rm det}$ (2)	z range (3)	$<\log L_{\rm AGN}>$ (4)	$<\log L_{\rm IR,SF}>$ (5)	$<\log M_{\rm BH}>$ (6)	$<ER>$ (7)
$L_{\rm AGN}$ bins						
43.0–43.5	13	0.200–0.430	$43.33^{+0.30}_{-0.17}$	$44.96^{+0.69}_{-1.39}$	$6.33^{+0.09}_{-0.06}$	$0.06^{+0.03}_{-0.02}$
43.5–44.0	17	0.208–0.593	$43.80^{+0.28}_{-0.17}$	$44.80^{+0.82}_{-1.19}$	9.75	...
44.0–44.5	51	0.205–0.900	$44.28^{+0.28}_{-0.21}$	$45.24^{+1.77}_{-1.25}$	$7.43^{+1.26}_{-1.74}$	$0.29^{+0.29}_{-0.65}$
44.5–45.0	49	0.238–1.730	$44.76^{+0.26}_{-0.24}$	$45.66^{+0.87}_{-0.79}$	$8.10^{+1.01}_{-1.15}$	$0.07^{+0.07}_{-0.27}$
45.0–45.5	66	0.310–2.261	$45.25^{+0.25}_{-0.25}$	$45.89^{+1.73}_{-1.24}$	$8.25^{+0.85}_{-1.13}$	$0.12^{+0.11}_{-0.41}$
45.5–46.0	71	0.316–2.447	$45.75^{+0.24}_{-0.25}$	$46.24^{+2.97}_{-0.76}$	$8.58^{+0.58}_{-0.52}$	$0.17^{+0.15}_{-0.49}$
46.0–46.5	37	0.776–2.301	$46.18^{+0.17}_{-0.29}$	$46.51^{+1.90}_{-0.68}$	$8.97^{+0.57}_{-0.71}$	$0.17^{+0.15}_{-0.22}$
46.5–47.0	14	1.077–2.452	$46.65^{+0.14}_{-0.20}$	$46.65^{+0.91}_{-0.70}$	$9.13^{+0.58}_{-0.31}$	$0.32^{+0.21}_{-0.49}$
$L_{\rm IR,\,SF}$ bins						
44.0–44.5	14	0.203–0.457	$43.81^{+0.55}_{-1.47}$	$44.34^{+0.23}_{-0.15}$	$7.00^{+0.76}_{-0.76}$	$0.05^{+0.03}_{-0.03}$
44.5–44.0	30	0.200–0.793	$44.36^{+1.20}_{-1.71}$	$44.78^{+0.27}_{-0.21}$	$7.43^{+1.26}_{-1.95}$	$0.41^{+0.40}_{-0.53}$
45.0–45.5	55	0.225–1.034	$44.66^{+1.39}_{-1.37}$	$45.27^{+0.27}_{-0.23}$	$7.67^{+1.32}_{-0.85}$	$0.11^{+0.10}_{-0.23}$
45.5–45.0	65	0.343–1.482	$44.95^{+1.58}_{-1.56}$	$45.77^{+0.27}_{-0.22}$	$8.27^{+0.87}_{-1.47}$	$0.13^{+0.13}_{-0.39}$
46.0–46.5	95	0.249–1.842	$45.48^{+2.45}_{-1.54}$	$46.26^{+0.25}_{-0.23}$	$8.51^{+2.12}_{-0.75}$	$0.12^{+0.12}_{-0.26}$
46.5–46.0	49	1.078–2.447	$46.06^{+0.65}_{-0.96}$	$46.74^{+0.23}_{-0.26}$	$8.80^{+0.79}_{-0.60}$	$0.23^{+0.19}_{-0.57}$
47.0–47.5	10	1.507–2.452	$46.32^{+0.83}_{-0.53}$	$47.13^{+0.09}_{-0.22}$	$9.27^{+0.71}_{-0.41}$	$0.12^{+0.10}_{-0.13}$

Notes. (1) Luminosity range in erg s^{-1}, (2) number of IR-bright AGNs in the selected bin, excluding SFR=0 objects, (3) redshift range for objects in the bin, (4) average AGN bolometric luminosity in erg s^{-1}, (5) average AGN-removed IR luminosity in erg s^{-1}, (6) average SMBH mass in $M_\odot$ for the subsample in the bin with a mass estimate, (7) average Eddington ratio for the subsample in the bin with a mass estimate. The errors in column (4)–(7) indicate the range for the binned objects.

has been suggested that using an instantaneous X-ray luminosity could lead to large scatter which smears out any intrinsic AGN–SF correlation (e.g. Hickox et al. 2014). Several studies have used the average X-ray or AGN luminosities and observed a positive correlation between AGN and SFR (Chen et al. 2013, 2015; Azadi et al. 2015). Binning the data by different criteria not only loses information from the data set, but also projects any intrinsic $L_{\rm AGN}$–SFR relation onto a specific axis, affecting the apparent slope of any correlation (Volonteri et al. 2015b). We thus choose not to bin the data in our analysis (Sections 4.1 and 4.2). When stacking data below the detection limit, the average values are biased by the outliers in each bin, especially when stacking a relatively small

number of non-detections. Instead, we defined an expanded sample which includes X-ray-detected sources with 'marginal' detections in the IR (see Section 2), extending below the flux limit to include fainter IR sources. This allows us to probe below the formal flux limit while including as much information as possible from the expanded sample. In our main sample, the average and median in each luminosity bin are statistically identical based on the K-S test result (Table 6).

In Fig. 5, we compare the best-fitting correlations based on different binning methods to test the variability scenario (Volonteri et al. 2015a). In red is the average $L_{\rm AGN}$ binned by $L_{\rm IR,SF}$, and in blue is the average $L_{\rm IR,SF}$ binned by $L_{\rm AGN}$. Both show a positive correlation with $P < 0.000001$). The average relation binned by $L_{\rm AGN}$ (blue line, slope $k = 0.59 \pm 0.17$) agrees well with the correlation without binning (dot-dashed black line, $k = 0.62 \pm 0.05$). Compared to the $L_{\rm AGN}$ bins, a strong correlation with a steeper slope is observed using $L_{\rm IR,SF}$ bins ($k = 1.11 \pm 0.19$). This effect is also seen in the Azadi et al. (2015) results (dark green stars in Fig. 5).

This slope change is a natural result of running a correlation test assuming a different dependent variable, but a similar change is also predicted by the more rapid variability of the AGN (Section 4.2), which explains the lack of the AGN–SF correlation for samples that are mass or SFR selected (e.g. Volonteri et al. 2015b). Unfortunately, the degeneracy in both time-scale and amplitude variation in the simulations, as well as the large uncertainties in the observed luminosities, makes it difficult to predict on a quantitative basis how much of the slope change is due to variability effect. Future simulation work is needed to test the relative statistical and variability contributions to the change in slope.

4.4 The ratio between SFR and BHAR

To test if the AGN–SF relation evolves with redshift or $M_\bullet$, in this section we compare the relative strength of SF and AGN, represented by the ratio of $L_{\rm IR,SF}$ and $L_{\rm X}$. We find that the luminosity ratio does not evolve with redshift or $M_\bullet$. Up to $z = 2.5$, the main sample shows a non-zero ratio of:

$$\log({\rm SFR/BHAR}) = (3.15 \pm 0.07) + (0.11 \pm 0.06)z \quad (5)$$

with a standard deviation of 0.50 (Fig. 7a). We also compare the ratios for the subsample of broad-lined AGNs with a secure $M_\bullet$ estimate (Fig. 7c). Despite the incompleteness of low-luminosity objects at high z, SFR/BHAR shows an overall constant ratio across $M_\bullet$:

$$\log({\rm SFR/BHAR}) = (3.79 \pm 0.65) - (0.06 \pm 0.08)\log({\rm M_\bullet/M_\odot}) \quad (6)$$

with a standard deviation of 0.52. This confirms the correlation between AGN and SF in the IR-bright AGN phase.

These results are consistent with the scenario in which both SF and SMBH growth are dependent upon a common gas supply that feeds the AGN-host system. Candidate sources of the gas supply are: mergers, cosmic cold flows, or secular evolution (e.g. Di Matteo et al. 2005; Mullaney et al. 2012b; Padovani et al. 2017). Although we cannot distinguish the source of the gas reservoir, the correlation indicates that for IR-active AGNs, both the core and the surrounding SF – local/circumnuclear or on the galaxy scale – are growing in tandem on a cosmological basis. High-resolution imaging is needed to trace the location of the SF. For our low-z and high-z subsamples, the wide luminosity range, non-zero correlation slope, and large scatter indicate that there may be a mixture of major mergers and isolated galaxies.

Our results are also in general agreement with Mullaney et al. (2012b, M12), despite the different sample selections. The M12 sample consists of stacks from star-forming galaxies that are both X-ray detected (∼20 per cent) and undetected (∼80 per cent). Although the majority of the M12 sample have no X-ray detection, a similar flat SFR/BHAR ratio was reported, with a constant value not evolving with redshift or stellar mass, consistent with our results. Compared to M12 (207 X-ray detections + 1037 X-ray non-detections), we have a larger sample with X-ray detections (323 + 33 supplementary), plus the expanded sample of 558 AGNs below the formal IR flux limit. At similar SFR, X-ray undetected targets have relatively lower BHAR and can drive the SFR/BHAR ratio higher, as confirmed by the higher mean ratio in M12, where log(SFR/BHAR) = 3.2–3.5. On the other hand, at similar X-ray luminosity, the inclusion of sources that are not detected in the IR would lower the SFR/BHAR ratio, as demonstrated later with our combined sample. Regardless of the sample used, this growth ratio of log(SFR/BHAR) ∼ 3 is constant over redshift, and dominates the final mass ratios if integrated over a long enough accretion history, thus leading to the locally observed mass ratios at log $(M_*/{\rm M_\bullet}) \sim 3$ (e.g. Merritt & Ferrarese 2001; McLure & Dunlop 2002; Marconi & Hunt 2003, see also equation 7 of M12).

A similar result of constant SFR/BHAR ratios, independent of redshift, was reported in Silverman et al. (2009), though with a 10 times lower log(SFR/BHAR) ratio at ∼2. Since the sample selection (X-ray luminosity-based) and SFR estimates ([OII] emission line-based) are distinctively different from this work, it is difficult to compare the results directly. Constant SFR/BHAR ratios have also been predicted by simulations, where the galaxy and BH can be modulated by torque-limited growth along the bulge-BH mass plane from $z = 4$ to $z = 0$ (e.g. Anglés-Alcázar et al. 2015), though large scatter and distinct variations are often noticed (e.g. Thacker et al. 2014; McAlpine et al. 2017).

To check for Malmquist bias, we also fit the SFR/BHAR versus z and $M_\bullet$ for the main + expanded combined sample (Figs 7b and d). The resulting average ratios in log scale are (2.89 ± 0.05) for SFR/BHAR versus z, and (3.18 ± 0.49) for SFR/BHAR versus $M_\bullet$. Using the expanded sample alone results in similar log ratios: (2.89 ± 0.05) for SFR/BHAR versus z, and (3.15 ± 0.07) for SFR/BHAR versus $M_\bullet$, consistent with the main sample results within errors. Both relations have a standard deviation of 0.55. We note that at a given $L_{\rm IR,SF}/L_{\rm X}$ or SFR/BHAR ratio, the AGN contribution to the total IR luminosity ($f = L_{\rm IR,AGN}/L_{\rm IR}$, see Fig. 3 and Section 3.1) ranges from insignificant ($f_{\rm AGN} < 0.2$) to dominant ($f_{\rm AGN} > 0.5$).

The mean SFR/BHAR ratio is consistent with the ratio of stellar to SMBH mass seen in local galaxies. The BH-host bulge mass relation is well-established at low z for AGNs: log $(M_{\rm bulge}/{\rm M_\bullet}) = 2.81 \pm 0.36$ (Marconi & Hunt 2003), log $(M_{\rm bulge}/{\rm M_\bullet}) = 2.90 \pm 0.45$ (Merritt & Ferrarese 2001; McLure & Dunlop 2002). Assuming the log $(M_{\rm bulge}/M_{*,\,\rm total})$ ratio is around −0.15 (Mendel et al. 2014, median for 660000 SDSS DR7 galaxies), we convert the BH-bulge relation to log $(M_*/{\rm M_\bullet}) = (2.96 \pm 0.36)$ and log $(M_*/{\rm M_\bullet}) = (3.05 \pm 0.45)$ (blue and green dashed lines in Fig. 7), both consistent with equation (5). Although IR-detected and undetected AGNs are reported to have similar host galaxy stellar masses (e.g. Rovilos et al. 2012; Santini et al. 2012; Rosario et al. 2013a), significantly different log $(M_*/{\rm M_\bullet})$ ratios from those quoted above have also been reported [e.g. 2.6 ± 0.4 in Kormendy & Ho (2013), and 3.6 ± 0.5 (Reines & Volonteri 2015)]. The difference in the accumulated mass ratios is sample dependent, and varies, from high to low, across quiescent, bulgeless/pseudo-

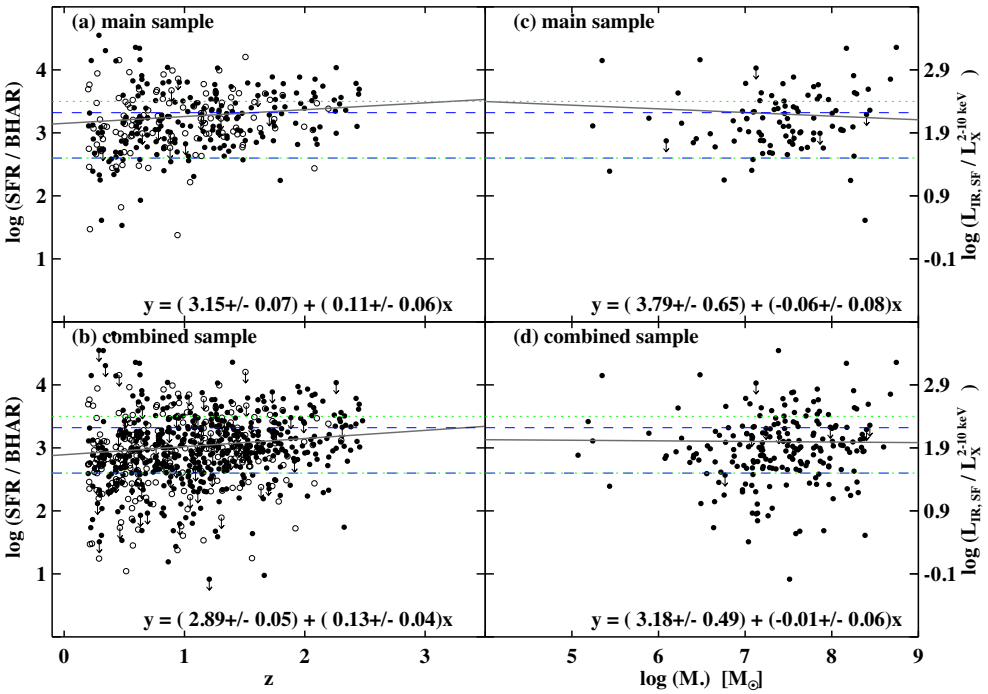

Figure 7. The log (SFR/BHAR) ratios as a function of redshift (a and b) and SMBH (c and d) for the main sample and the combined sample (main + expanded). Only type 1 AGNs with an $M_\bullet$ estimate are included in the right-hand panels. On the right-hand *y*-axis we mark the values of corresponding $L_{\rm IR,SF}$ and hard X-ray luminosity $L_{\rm X}$ ratios. Filled and open circles mark the type 1 (optical broad emission line or X-ray unobscured) and type 2 (optical narrow line or X-ray obscured) objects, respectively. The solid lines are the linear fits to the IR-bright AGN sample, with the fitted function marked in each panel. We observe a mean ratio of ∼3 for the mass formation/accretion ratios log (SFR/BHAR). The intrinsic scatters (standard deviation) are 0.50 (a), 0.55 (b), 0.51(c), and 0.55 (d), respectively. Inclusion of the $z < 0.2$ and $z > 2.5$ supplementary sample yields consistent results (not plotted). The dashed blue lines mark the $\pm 1\sigma$ range of the $M_*/M_\bullet$ ratios from Marconi & Hunt (2003), and the dotted green lines mark the range in Merritt & Ferrarese (2001) and McLure & Dunlop (2002).

bulges, classical giant elliptical and bulge galaxies (Kormendy & Ho 2013).

Compared to the literature values for log ($M_*/M_\bullet$) (e.g. blue and green lines in Fig. 7), our sample shows a larger scatter (0.50 versus 0.36 in Marconi & Hunt (2003), versus 0.45 in Merritt & Ferrarese (2001); McLure & Dunlop (2002), all in log scale). This is due to one or more of the following factors: (a) the uncertainties in the SFR and BHAR estimates; (b) the large range of the instantaneous ratios due to rapid AGN variability; (c) the unknown host galaxy morphology – our sample is not restricted to bulges or ellipticals, and could include spirals and other type of galaxies that may not share the same mass ratios. However, the mean SFR/BHAR ratio is not related to mass or redshift (Fig. 7), indicating that for objects with currently active growth of black hole and SF, the central BH and the stellar mass grow at a similar rate on average. The large scatter in the mass ratios is likely the result of the different evolutionary paths and stages of the AGN systems in the sample.

5 SUMMARY

We have constructed a sample of 323 IR-bright AGNs with $L_{\rm X} > 10^{42}$erg s^{-1} at $0.2 < z < 2.5$ in the ∼11 deg^2 *XMM*–LSS field (the main sample). All targets are detected in both hard X-ray and FIR with either spectroscopic or photometric redshift measurements. The majority of the sample (65 per cent) are type 1 objects, and 86 per cent have dust mass greater than 10^8 M$_\odot$. This IR-bright AGN sample is thus dominated by type 1 AGNs with significant dust and SF in the AGN-host system. For comparison, and to expand the luminosity parameter space, we also construct an expanded sample of 558, X-ray AGNs with 1–3σ IR detections, formally undetected; and a supplementary sample of 33, $z < 0.2$ or $z > 2.5$ IR-bright AGNs. Our main results are summarized as follows:

(i) We find significant bivariate AGN–SF correlations between the absorption-corrected X-ray luminosity and total IR luminosities for the IR-bright AGN main sample, including integrated luminosities $L_{\rm IR}$ (8–1000 μm), $L_{\rm FIR}$ (30–1000 μm), and at individual wavelengths (L_{60}, L_{100}). The $L_{\rm IR,SF}$ and $L_{\rm AGN}$ correlation has a power-law slope of (0.62 ± 0.05), and a probability of $P < 0.0001$. This slope does not vary significantly towards fainter flux-limits.

(ii) We find that AGN can contribute significantly to the IR and FIR fluxes and luminosities, and this contribution ranges from negligible up to almost 100 per cent. On average, the AGN contributions to the total IR luminosity (8–1000 μm) are 11 per cent for the main sample, and 23 per cent for the expanded sample. The total $L_{\rm FIR}^{300-1000}$ is consistent with the AGN-removed $L_{\rm IR,SF}$ within the errors for >92 per cent of the main sample, and can be used as a proxy for $L_{\rm IR,SF}$. We find that single-band luminosity at longer wavelengths (L_{60} and L_{100}) suffers the least AGN contamination (∼2 per cent).

(iii) The application of a partial correlation test (PSRA) to determine the dominant variable for the main sample leads to the conclusion that the bivariate AGN–IR correlations are primarily driven by redshift (Table 5).

(iv) Binning the data by either IR or X-ray luminosity affects the observed correlation significance and slopes.

(v) Using L_{60} and L_{100}, as proxies for SF, PSRA tests reveal a strong residual AGN–SF correlation with a slope of ∼0.2 and high

significance ($P < 0.005$), beyond that resulting from the redshift in our combined sample (main + expanded). The lack of a correlation when using $L_{\rm IR,SF}$ is likely a result of the large uncertainties in the AGN-subtraction.

(vi) Significant, flatter ($\alpha \sim 0.2$) $L_{\rm AGN}$–$L_{\rm IR,SF}$ correlations are found in three of four subsamples covering a smaller redshift range (so as to reduce the redshift effect). The correlation significance increases when the expanded sample is also included. However, the large scatter and small subsamples result in large errors on the derived slopes. A larger IR-detected sample with a wider IR luminosity range at each redshift will be valuable to confirm these results. While we see no evidence for SF being quenched by AGN activity, it remains possible that this occurs on significantly different time-scales than probed by our study.

(vii) There is no evidence that the relationship between AGN luminosity and IR luminosity changes with black hole mass or Eddington ratios.

(viii) The average ratio of the SF and BH accretion rate is: log (SFR/BHAR) ~ 3.15, with a deviation of 0.50 ($\sim 2.89 \pm 0.55$ for the combined sample), independent of redshift or SMBH mass, but with a wide dispersion. The average SFR/BHAR ratio is consistent with the mean observed $M_*/M_\bullet$ ratio found in local galaxies. The consistent averages support a scenario in which a SMBH and its host galaxy both grow from a common gas supply, when averaged over long time periods. Unlike earlier results that suggested two formation paths (e.g. Lutz et al. 2010; Shao et al. 2010; Rosario et al. 2012; Santini et al. 2012), our overall correlation combined with the similar results in different redshift bins, suggest that it is not likely that AGN and SF are completely unrelated, nor that they are dominated by feedback in which an AGN quenches the SF.

ACKNOWLEDGEMENTS

We thank the anonymous referee for constructive and detailed comments that improved and clarified this paper.

YSD would like to thank Lee Armus, Nick Scoville, Phillip Hopkins, Chris Hayward, Xiangcheng Ma, and Ranga R. Chary for helpful discussions. BJW gratefully acknowledged the support of NASA Contract NAS8-03060 (CXC).

This work is sponsored in part by the Chinese Academy of Sciences (CAS), through a grant to the CAS South America Center for Astronomy (CASSACA) based in Santiago, Chile. This research has made use of data from HerMES project (http://hermes.sussex.ac.uk/). HerMES is a Herschel Key Programme utilizing Guaranteed Time from the SPIRE instrument team, ESAC scientists and a mission scientist. The HerMES data was accessed through the Herschel Database in Marseille (HeDaM - http://hedam.lam.fr) operated by CeSAM and hosted by the Laboratoire d'Astrophysique de Marseille.

REFERENCES

Aird J., Coil A. L., Georgakakis A., Nandra K., Barro G, Pérez-González P. G., 2015, MNRAS, 451, 1892
Akritas M. G., Siebert J., 1996, MNRAS, 278, 919
Alexander D. M., Hickox R. C., 2012, New Astron. Rev., 56, 93
Alton P. B., Xilouris E. M., Misiriotis A., Dasyra K. M., Dumke M., 2004, A&A, 425, 109
Anglés-Alcázar D., Özel F., Davé R., Katz N., Kollmeier J. A., Oppenheimer B. D., 2015, ApJ, 800, 127
Antonucci R. R. J., Miller J. S., 1985, ApJ, 297, 621
Aversa R., Lapi A., de Zotti G., Shankar F., Danese L., 2015, ApJ, 810, 74
Azadi M. et al., 2015, ApJ, 806, 187
Azadi M. et al., 2017, ApJ, 835, 27
Barger A. J., Cowie L. L., Owen F. N., Chen C.-C., Hasinger G., Hsu L.-Y., Li Y., 2015, ApJ, 801, 87
Barthel P. D., 1989, ApJ, 336, 606
Beelen A., Cox P., Benford D. J., Dowell C. D., Kovács A., Bertoldi F., Omont A., Carilli C. L., 2006, ApJ, 642, 694
Bentz M. C. et al., 2013, ApJ, 767, 149
Bernhard E., Mullaney J. R., Daddi E., Ciesla L., Schreiber C., 2016, MNRAS, 460, 902
Blain A. W., Barnard V. E., Chapman S. C., 2003, MNRAS, 338, 733
Bournaud F., Dekel A., Teyssier R., Cacciato M., Daddi E., Juneau S., Shankar F., 2011, ApJ, 741, L33
Bower R. G., Benson A. J., Malbon R., Helly J. C., Frenk C. S., Baugh C. M., Cole S., Lacey C. G., 2006, MNRAS, 370, 645
Brightman M. et al., 2016, ApJ, 826, 93
Chen C.-T. J. et al., 2013, ApJ, 773, 3
Chen C.-T. J. et al., 2015, ApJ, 802, 50
Chen C.-T. J. et al., 2017, ApJ, 837, 145
Chiappetti L. et al., 2013, MNRAS, 429, 1652
Croom S. M. et al., 2009, MNRAS, 399, 1755
Dai Y. S. et al., 2012, ApJ, 753, 33
Dai Y. S. et al., 2014, ApJ, 791, 113
Dale D. A., Helou G., Magdis G. E., Armus L., Díaz-Santos T., Shi Y., 2014, ApJ, 784, 83
Debuhr J., Quataert E., Ma C.-P., 2012, MNRAS, 420, 2221
Dekel A. et al., 2009, Nature, 457, 451
Di Matteo T., Springel V., Hernquist L., 2005, Nature, 433, 604
Diamond-Stanic A. M., Rieke G. H., 2012, ApJ, 746, 168
Elbaz D. et al., 2007, A&A, 468, 33
Elbaz D. et al., 2011, A&A, 533, A119
Elvis M. et al., 1994, ApJS, 95, 1
Esquej P. et al., 2014, ApJ, 780, 86
Fabian A. C., 2012, ARA&A, 50, 455
Fanidakis N. et al., 2012, MNRAS, 419, 2797
Ferrarese L., Merritt D., 2000, ApJ, 539, L9
Fiore F. et al., 2009, ApJ, 693, 447
Fu H. et al., 2010, ApJ, 722, 653
Gabor J. M., Bournaud F., 2013, MNRAS, 434, 606
Gandhi P., Horst H., Smette A., Hönig S., Comastri A., Gilli R., Vignali C., Duschl W., 2009, A&A, 502, 457
García-González J. et al., 2016, MNRAS, 458, 4512
Goulding A. D., Alexander D. M., Bauer F. E., Forman W. R., Hickox R. C., Jones C., Mullaney J. R., Trichas M., 2012, ApJ, 755, 5
Greene J. E., Ho L. C., 2005, ApJ, 630, 122
Harris K. et al., 2016, MNRAS, 457, 4179
Harrison C. M. et al., 2012, ApJ, 760, L15
Hasinger G., 2008, A&A, 490, 905
Heckman T. M., Best P. N., 2014, ARA&A, 52, 589
Hickox R. C., Mullaney J. R., Alexander D. M., Chen C.-T. J., Civano F. M., Goulding A. D., Hainline K. N., 2014, ApJ, 782, 9
Hopkins P. F., 2012, MNRAS, 420, L8
Hopkins P. F., Hernquist L., Cox T. J., Di Matteo T., Robertson B., Springel V., 2006, ApJS, 163, 1
Hopkins P. F., Torrey P., Faucher-Giguère C.-A., Quataert E., Murray N., 2016, MNRAS, 458, 816
Isobe T., Feigelson E. D., Nelson P. I., 1986, ApJ, 306, 490
Kaspi S., Smith P. S., Netzer H., Maoz D., Jannuzi B. T., Giveon U., 2000, ApJ, 533, 631
Keel W. C. et al., 2012, MNRAS, 420, 878
Kendall M., Stuart A., 1976, The Advanced Theory of Statistics, 3rd edn. Griffin, London
Kennicutt R. C., Jr., 1998, ARA&A, 36, 189
Klypin A. A., Trujillo-Gomez S., Primack J., 2011, ApJ, 740, 102
Kormendy J., Ho L. C., 2013, ARA&A, 51, 511
Kormendy J., Richstone D., 1995, ARA&A, 33, 581
Krawczyk C. M., Richards G. T., Mehta S. S., Vogeley M.S., Gallagher S. C., Leighly K. M., Ross N. P., Schneider D. P., 2013, ApJS, 206, 4
Lansbury G. B. et al., 2015, ApJ, 809, 115

Lansbury G. B. et al., 2017, ApJ, 836, 99
Lanzuisi G., Piconcelli E., Fiore F., Feruglio C., Vignali C., Salvato M., Gruppioni C., 2009, A&A, 498, 67
Lapi A., Raimundo S., Aversa R., Cai Z.-Y., Negrello M., Celotti A., De Zotti G., Danese L., 2014, ApJ, 782, 69
Lavalley M. P., Isobe T., Feigelson E. D., 1992, BAAS, 24, 839
Lilly S. J., Carollo C. M., Pipino A., Renzini A., Peng Y., 2013, ApJ, 772, 119
Luo B. et al., 2017, ApJS, 228, 2
Lutz D., Maiolino R., Spoon H. W. W., Moorwood A. F. M., 2004, A&A, 418, 465
Lutz D. et al., 2010, ApJ, 712, 1287
Madau P., Dickinson M., 2014, ARA&A, 52, 415
Magorrian J. et al., 1998, AJ, 115, 2285
Mancuso C., Lapi A., Shi J., Gonzalez-Nuevo J., Aversa R., Danese L., 2016, ApJ, 823, 128
Marconi A., Hunt L. K., 2003, ApJ, 589, L21
Marconi A., Risaliti G., Gilli R., Hunt L. K., Maiolino R., Salvati M., 2004, MNRAS, 351, 169
Mateos S. et al., 2015, MNRAS, 449, 1422
Matsuoka K., Woo J.-H., 2015, ApJ, 807, 28
McAlpine S. et al., 2017, MNRAS, 468, 3395
McLean I. S. et al., 2012, Proc. SPIE, 8446, 84460J
McLure R. J., Dunlop J. S., 2002, MNRAS, 331, 795
McLure R. J., Dunlop J. S., 2004, MNRAS, 352, 1390
Melnyk O. et al., 2013, A&A, 557, A81
Mendel J. T., Simard L., Palmer M., Ellison S. L., Patton D. R., 2014, ApJS, 210, 3
Merloni A., Rudnick G., Di Matteo T., 2004, MNRAS, 354, L37
Merritt D., Ferrarese L., 2001, MNRAS, 320, L30
Moustakas J. et al., 2013, ApJ, 767, 50
Mullaney J. R., Alexander D. M., Goulding A. D., Hickox R. C., 2011, MNRAS, 414, 1082
Mullaney J. R. et al., 2012a, MNRAS, 419, 95
Mullaney J. R. et al., 2012b, ApJ, 753, L30
Naab T., Ostriker J. P., 2017, ARA&A, 55, 59
Netzer H., 2009, MNRAS, 399, 1907
Netzer H. et al., 2007, ApJ, 666, 806
Noeske K. G. et al., 2007, ApJ, 660, L43
Oliver S. J. et al., 2012, MNRAS, 424, 1614
Padovani P. et al., 2017, A&A Rev., 25, 2
Page M. J. et al., 2012, Nature, 485, 213
Pannella M. et al., 2009, ApJ, 698, L116
Pierre M. et al., 2007, MNRAS, 382, 279
Pitchford L. K. et al., 2016, MNRAS, 462, 4067
Podigachoski P. et al., 2015, A&A, 575, A80
Priddey R. S., Isaak K. G., McMahon R. G., Omont A., 2003, MNRAS, 339, 1183
Ranalli P., Comastri A., Setti G., 2003, A&A, 399, 39
Ranalli P. et al., 2016, A&A, 590, A80
Reines A. E., Volonteri M., 2015, ApJ, 813, 82
Richards G. T. et al., 2006, ApJS, 166, 470
Rodighiero G. et al., 2011, ApJ, 739, L40
Rosario D. J. et al., 2012, A&A, 545, A45
Rosario D. J. et al., 2013a, ApJ, 771, 63
Rosario D. J. et al., 2013b, A&A, 560, A72
Roseboom I.G. et al., 2010, MNRAS, 409, 48
Roseboom I.G. et al., 2012, MNRAS, 419, 2758
Rovilos E. et al., 2012, A&A, 546, A58
Santini P. et al., 2012, A&A, 540, A109
Shao L. et al., 2010, A&A, 518, L26
Shen Y. et al., 2011, ApJS, 194, 45
Shimizu T. T., Mushotzky R. F., Meléndez M., Koss M., Rosario D. J., 2015, MNRAS, 452, 1841
Shimizu T. T., Meléndez M., Mushotzky R. F., Koss M. J., Barger A. J., Cowie L. L., 2016, MNRAS, 456, 3335
Shimizu T. T., Mushotzky R. F., Meléndez M., Koss M. J., Barger A. J., Cowie L. L., 2017, MNRAS, 466, 3161
Siebenmorgen R., Krügel E., 2007, A&A, 461, 445
Silk J., Rees M. J., 1998, A&A, 331, L1
Silverman J. D. et al., 2008, ApJ, 679, 118
Silverman J. D. et al., 2009, ApJ, 696, 396
Speagle J. S., Steinhardt C. L., Capak P. L., Silverman J. D., 2014, ApJS, 214, 15
Springel V. et al., 2005, Nature, 435, 629
Stanley F., Harrison C. M., Alexander D. M., Swinbank A. M, Aird J. A, Del Moro A., Hickox R. C., Mullaney J. R., 2015, MNRAS, 453, 591
Stanley F. et al., 2017, MNRAS, 472, 2221
Stern D., 2015, ApJ, 807, 129
Symeonidis M. et al., 2011, MNRAS, 417, 2239
Szokoly G. P. et al., 2004, ApJS, 155, 271
Thacker R. J., MacMackin C., Wurster J., Hobbs A., 2014, MNRAS, 443, 1125
Treister E., Schawinski K., Urry C. M., Simmons B. D., 2012, ApJ, 758, L39
Vasudevan R. V., Fabian A. C., 2007, MNRAS, 381, 1235
Vestergaard M., Peterson B. M., 2006, ApJ, 641, 689
Volonteri M., Capelo P. R., Netzer H., Bellovary J., Dotti M., Governato F., 2015a, MNRAS, 449, 1470
Volonteri M., Capelo P. R., Netzer H., Bellovary J., Dotti M., Governato F., 2015b, MNRAS, 452, L6
Wang L. et al., 2014, MNRAS, 444, 2870
Wilkes B. J. et al., 2013, ApJ, 773, 15
Xu L., Rieke G. H., Egami E., Haines C. P, Pereira M. J., Smith G. P., 2015a, ApJ, 808, 159
Xu L., Rieke G. H., Egami E., Pereira M. J., Haines C. P., Smith G. P., 2015b, ApJS, 219, 18
Yang G. et al., 2017, ApJ, 842, 72

SUPPORTING INFORMATION

Supplementary data are available at *MNRAS* online.

Table S1: table2.ascii
Table S2. Derived properties for IR-bright AGNs.
Please note: Oxford University Press is not responsible for the content or functionality of any supporting materials supplied by the authors. Any queries (other than missing material) should be directed to the corresponding author for the article.

This paper has been typeset from a TEX/LATEX file prepared by the author.